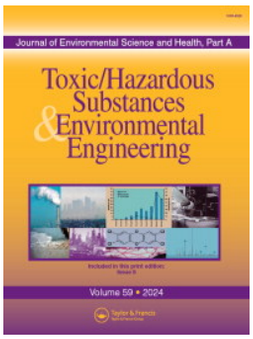

Taylor & Francis
Taylor & Francis Group

Journal of Environmental Science and Health, Part A
Toxic/Hazardous Substances and Environmental Engineering

ISSN: (Print) (Online) Journal homepage: www.tandfonline.com/journals/lesa20

Preparation and characterization of β-cyclodextrin capped magnetic nanoparticles anchored on cellulosic matrix for removal of cr(VI) from mimicked wastewater: Adsorption and kinetic studies

Lynda S. Mesoppirr, Evans K. Suter, Wesley N. Omwoyo, Nathan M. Oyaro & Simphiwe M. Nelana

To cite this article: Lynda S. Mesoppirr, Evans K. Suter, Wesley N. Omwoyo, Nathan M. Oyaro & Simphiwe M. Nelana (07 Nov 2024): Preparation and characterization of β-cyclodextrin capped magnetic nanoparticles anchored on cellulosic matrix for removal of cr(VI) from mimicked wastewater: Adsorption and kinetic studies, Journal of Environmental Science and Health, Part A, DOI: 10.1080/10934529.2024.2424084

To link to this article: https://doi.org/10.1080/10934529.2024.2424084

Published online: 07 Nov 2024.

JOURNAL OF ENVIRONMENTAL SCIENCE AND HEALTH, PART A
https://doi.org/10.1080/10934529.2024.2424084

Preparation and characterization of β-cyclodextrin capped magnetic nanoparticles anchored on cellulosic matrix for removal of cr(VI) from mimicked wastewater: Adsorption and kinetic studies

Lynda S. Mesoppirr[a], Evans K. Suter[a,b], Wesley N. Omwoyo[a,b], Nathan M. Oyaro[a], and Simphiwe M. Nelana[b]

[a]Department of Mathematics and Physical Science, Maasai Mara University, Narok, Kenya; [b]Biotechnology and Chemistry Department, Vaal University of Technology, Vanderbijlpark, South Africa

ABSTRACT

Hexavalent Chromium (Cr(VI)) is essential in many industrial processes. However, it finds its way into water bodies, posing health problems, including lung cancer and the inhibition of DNA and RNA in biological systems. Several chemical and traditional water purification methods have been developed in the past, but most are expensive, tedious and ineffective. This study aimed to prepare and characterize a low-cost hybrid adsorbent, β-Cyclodextrin capped magnetic nanoparticles anchored on a cellulosic matrix (CNC-Fe_3O_4NP-CD). The characterization techniques confirmed the integration of CNCs, Fe_3O_4NP and CD into the prepared CNC-Fe_3O_4NP-CD nanocomposite adsorbent. The adsorbent was employed in batch adsorption experiments by varying adsorption parameters, including solution pH, adsorbent dosage, initial Cr(VI) concentration, and contact time. From the findings, the nanocomposite adsorbent achieved a maximum Cr(VI) removal efficiency of 97.45%, while the pseudo-second-order kinetic model best fitted the experimental data with high linear regression coefficients ($R^2 >$ 0.98). The Elovich model indicated that the adsorption process was driven by chemisorption on heterogeneous surface sites, with initial sorption rates surpassing desorption rates. These findings established that CNC-Fe_3O_4NP-CD presents high efficiency for Cr(VI) removal under acidic pH, offering the potential for optimization and application in real-world wastewater treatment.

ARTICLE HISTORY
Received 15 September 2024
Accepted 28 October 2024

KEYWORDS
Typha angustifolia; adsorption; wastewater treatment; hexavalent chromium; nanocomposite; kinetics

Introduction

Water is one of the most abundant features on Earth, covering up to 70% of Earth's crust.[1] Unfortunately, less than 1% of this water is fit for human consumption due to pollution.[2–4] Water pollution is the deterioration of water quality by organic and inorganic matter.[5] The inorganic pollutants include heavy metals, anions and ligands above permissible limits.[5] Heavy metals are metals with a density of about 4-7.5 g/mL and are toxic even at trace concentrations.[6] They include mercury, lead, chromium, cadmium, copper, arsenic, etc. and are associated with bioaccumulation in biological organisms.[7]

Heavy metal contamination exists in aqueous wastes in many industries, such as metal plating, mining operations, tanneries, radiator manufacturing, smelting, alloy industries, and storage batteries industries.[8] Excessive release of these heavy metals into the environment due to industrialization and urbanization has posed a significant problem worldwide.[9,10] Unlike organic pollutants, most susceptible to biological degradation, heavy metals do not degrade into harmless end products.[11] Various heavy metals have varying effects on humans; however, their presence in excess poses major concern due to their toxicity to many life forms.[12]

According to Hossini et al.[13] chromium (VI) is common in most plastic, leather and tannery industries, while chromium (III) is an essential element in the human body, commonly used in supplements and drugs. However, Cr(VI) is very toxic and can enter the human system through inhalation, ingestion or skin contact, causing lung cancer, nasal irritation, nasal ulcers, and hypersensitivity reactions, e.g. asthma and dermatitis.[11,13] It also inhibits biological systems' DNA, RNA and protein synthesis, inducing cell death.[13] This thus calls for the development of water treatment technologies that are efficient and inexpensive and can eliminate these heavy metals, especially chromium, even at trace levels.

Traditional wastewater treatment technologies, including distillation, chlorination, ion exchange resins, and membrane filtration, are commonly used to remove toxic metal ions from water. [14–17] However, these methods face several drawbacks, such as their effectiveness only at high pollutant concentrations, low surface active sites, high operational costs, and applicability mainly to small-scale filtrations.[18–20] Ion exchange resins, while useful, are easily fouled by organic impurities in wastewater, reducing their efficiency.[21] Membrane filtration methods like nanofiltration, ultrafiltration, and reverse osmosis are efficient but capital-intensive

CONTACT Wesley N. Omwoyo wesleyomwoyo@mmarau.ac.ke Department of Mathematics and Physical Science, Maasai Mara University. P.O Box 861-20500, Narok, Kenya

due to high maintenance costs associated with the necessary high pressures.[18,22]

Recently, physical heavy metals removal methods based on adsorption have been reported to be promising due to their simplicity, cost-effectiveness, and high adsorption capacity.[23] Some reported effective adsorbents include activated carbon, alumina, calcite, and polyaniline.[24] However, due to their bulky size, these materials often show limitations such as low adsorption capacities, expensive and limited regeneration, short lifespans, and high mass transfer resistance.[24] Therefore, designing cost-effective adsorbents like nanoparticles with high capacities and selectivity for specific pollutants is crucial for enhancing water treatment efficiency.[25]

Nanoparticles have been reported to be effective in removing heavy metals due to their high surface area-to-volume ratio, providing numerous adsorption sites.[25] However, nanoparticles, especially iron oxide nanoparticles, tend to agglomerate reducing their efficiency.[26] To prevent this, stabilizers, such as surfactants, bifunctional organic compounds, natural polymers, or biological materials, are used during the synthesis to prevent inter-particle interactions and aggregation by modifying the nanoparticle surfaces.[27] The choice of stabilizer, however, depends on the nanoparticle type and synthesis method. Proper surface modification with stabilizers ensures sufficient repulsive forces between particles, maintaining a stable suspension.[25,28,29] In this study, cyclodextrin was selected as the capping agent to enhance the stabilization of the magnetic iron oxide nanoparticles.

Cyclodextrin (CD) is a group of nontoxic polar cyclic oligosaccharides. They contain several glucose monomer units linked by α-(1,4) bonds, creating a cone-shaped compound.[30] Examples of CD include six-membered (α-cyclodextrin), seven-membered (β-cyclodextrin) and eight-membered (γ-cyclodextrin) ring units. β-cyclodextrin, however, has a unique characteristic of having both hydrophobic and hydrophilic sites and hence has the potential to be modified to adsorb a range of target pollutants.[31] Consequently, due to the high cost of β-cyclodextrin, this study sought to include inexpensive material to act as a matrix to the adsorbent. Some recommended inexpensive materials include cellulosic materials, chitosan, etc.[32,33] According to a study by Solhi et al.[34], the improved surface area to volume ratio and quantum size of CNCs increases the number of adsorption sites and the molecular tuning ability to change their surface features, making it a good choice for the bulk part of the composite matrix.

In this study, cellulose was extracted from Cattail grass (*Typhaceae angustifolia*) and used to prepare cellulose nanocrystals. *Typhaceae angustifolia* is a perennial wetland plant with a dense matrix of rhizomes and a well-developed aerenchyma system, allowing it to thrive in wetlands.[35,36] It is widely available in tropical wetlands and is often unused. Its fibrous and pulpy nature suggests a high cellulose content, making it a potential natural adsorbent for water pollution.[34]

This study thus prepared a hybrid nanocomposite adsorbent, β-Cyclodextrin capped magnetic nanoparticles anchored on a cellulosic matrix that is chemically specific and capable of permanently sequestering Cr(VI) ions from aqua media. From the literature survey, no work was reported on developing cellulose nanocrystals/magnetic iron oxide/β-Cyclodextrin nanocomposite adsorbent for Cr(VI) ions removal from synthetic, domestic and industrial wastewaters.

Materials and methods

Materials and chemicals

Typha angustifolia grass was harvested from the Maasai Mara University botanical garden in Narok, Kenya (1° 41′ 5.2872″ N and 37° 20′ 27.096″ E) at an altitude of 1827 meters above sea level. The approximately 4-meter-tall grass was cut, chopped into smaller pieces, washed with distilled water, and air-dried in the laboratory. It was then ground into fine powder and packed in sealed plastic bags, ready for dewaxing and delignification.[37]

Other chemicals and reagents used in the study were sodium hydroxide (NaOH ≥ 98%), sulfuric acid (H_2SO_4, >98%), acidified sodium hypochlorite (NaOCl, ≥75%), acetic acid (≥ 99%), acetone (≥99.9%), ammonium hydroxide (25%, NH_4OH), iron (III) chloride hexahydrate ($FeCl_3.6H_2O$ ≥99%), ferrous sulfate heptahydrate ($FeSO_4.7H_2O$) (≥99.5%), methanol (≥99.85%), distilled water, β-Cyclodextrin, potassium dichromate ($K_2Cr_2O_7$ >99%), hydrochloric acid (HCl ≥32%) and nitric acid (HNO_3 ≥55%). All the chemicals used were of analytical grade and were purchased from Sigma-Aldrich.

Methods

Extraction of cellulose from Typha angustifolia

The dewaxing and delignification of *Typha angustifolia* grass involved soaking 50 g of dried grass powder in 10% nitric acid at 80 °C for 2 h, followed by washing. An alkaline pretreatment was then conducted by mixing 50 g of the powder with 500 mL of 1.0 M NaOH in a reactor at 80 °C, stirred at 800 rpm for 3 h. The resulting cellulose fibers were quenched with cold deionized water, washed until neutral, and then stored for purification. Purification involved refluxing the cellulose fibers with 350 mL of 7.35% sodium hypochlorite and 4 mL acetic acid, agitated for 2 h at 80 °C with constant stirring at 500 rpm. The chemically purified cellulose was filtered, rinsed to neutral pH, treated with acetone in a Soxhlet chamber for 30 min to remove impurities, and dried at room temperature for three days.

Synthesis of nanocellulose

In a 500 mL conical flask, 20 g of chemically purified cellulose (CPC) was combined with 400 mL of 32% sulfuric acid, using a 1:20 ratio, and heated in a water bath, first to 45 °C, then to 55 °C with constant stirring at 600 rpm for 45 min. Hydrolysis was stopped by quenching with 200 mL of deionized water and repeated five times. The suspension was homogenized using a centrifuge at 10,000 rpm for 40 min, repeated five times until the supernatant was neutral. After drying for three days at room temperature, the resulting CNCs were packaged for characterization and subsequent experimental steps.

Functionalization of cellulose nanocrystals with iron oxide nanoparticles

For synthesizing Fe_3O_4 nanoparticles (Fe_3O_4NP), a co-precipitation method by Evans et al.[38] was adopted with slight modifications. First, an aqueous solution containing $FeCl_3{\cdot}6H_2O$ and $FeCl_2{\cdot}4H_2O$ in a 2:1 molar ratio was prepared. The solution was heated to 80 °C under nitrogen gas, and a 25% ammonia solution was added dropwise until the pH reached 10, forming Fe_3O_4NP. The black residue was washed with deionized water and ethanol and dried. To functionalize CNC with Fe_3O_4NP, a suspension of CNCs was mixed with the Fe_3O_4NP under ultrasonic agitation for 1 h to ensure uniform coating. The mixture was then stirred continuously at room temperature for 4 h. The resulting CNC iron oxide nanoparticle (CNC-Fe_3O_4NP) was separated using a magnet, washed with deionized water, and dried in a vacuum oven at 60 °C for 12 h.

Capping of cellulose nanocrystal/magnetic iron oxide nanoparticles with β-cyclodextrin

First, a solution of β-Cyclodextrin (β-CD) was prepared at room temperature by dissolving it in deionized water at 10 mg/mL until fully dissolved. The CNC-Fe_3O_4NP nanocomposite was dispersed in deionized water and sonicated for 30 min to form a homogeneous suspension. The β-CD solution was then added to the CNC-Fe_3O_4NP suspension with constant stirring. 0.1 M NaOH was added dropwise to the mixture to ensure successful capping. The reaction was maintained at 70 °C for *6 h* under continuous stirring. After the capping, the mixture was cooled to room temperature. The β-cyclodextrin capped cellulose nanocrystal/magnetic iron oxide nanoparticles (CNC-Fe_3O_4NP-CD) nanocomposite was separated using a magnet and washed several times with deionized water to remove any unreacted β-CD and other impurities. The CNC-Fe_3O_4NP-CD was then dried in a vacuum oven at 60 °C. The resulting CNC-Fe_3O_4NP-CD nanocomposite adsorbent was stored in airtight plastic bags for subsequent characterization and adsorption studies.

Characterization

Perkin Elmer Fourier Transform Infrared (FTIR) spectrometer was used to analyze the functional groups present in CPC, CNC, Fe_3O_4NP, CNC-Fe_3O_4NP, and CNC-Fe_3O_4NP-CD. The spectra of the samples were recorded in the range of 4000 to 500 cm^{-1} wavelength range. The resolution was set to 4 cm^{-1}, and 16 scans were accumulated for each spectrum. The spectrum was baseline corrected, normalized, and smoothened, and the key absorption peaks were identified.

Scanning electron microscopy- Energy Dispersive X-ray Spectroscopy (SEM-EDS, JEOL IT-7500LA) was employed to analyze the samples' surface morphology and elemental composition. SEM images were captured at an accelerating voltage of 15-20 kV. The samples were first coated with a thin layer of gold using a sputter coater to enhance conductivity. The scanning magnification ranged from 1,000x to 50,000x. The SEM images were mapped for elemental composition, and the spectra were collected at an accelerating voltage of 15 kV. The peaks corresponding to elements were then identified.

A vibrating sample magnetometer (VSM- Quantum Design PPMS VSM) was used to measure the magnetic strength of Fe_3O_4NP, CNC-Fe_3O_4NP and CNC- Fe_3O_4NP-CD. Approximately 50 mg of the sample was placed in a VSM sample holder. The magnetic hysteresis loops were recorded at room temperature, applying a magnetic field ranging from −15,000 Oe to +15,000 Oe.

X-ray diffraction (XRD- Shimadzu XRD-7000) was utilized to examine the crystalline structure of the materials. The powdered samples were placed on a sample holder, and XRD patterns were recorded. The diffractometer operated with Cu Kα radiation ($\lambda = 1.5406$ Å) at 40 kV and 30 mA. The scanning range (2θ) was set from 10° to 80° at a scanning rate of 2°/min. The obtained diffraction patterns were used to calculate the average particle sizes using the Scherrer equation (Eq. 1).[39]

$$Crystal\ size(\mathrm{D}) = \frac{\mathrm{K}\lambda}{\beta\ \mathrm{Cos}\ \theta} \tag{1}$$

where K(0.89) is the crystal structure factor, λ is the length of a light wave (1.54056 Å), β is the full width at half maximum (FWHM) in radians, and θ is the angle of diffraction in degrees.

Adsorption studies

Batch studies were conducted at 25 ± 1 °C to examine the adsorption behavior of CPC, CNC, CNC-Fe_3O_4NP and CNC-Fe_3O_4NP-CD toward removing Cr(VI) from aqueous media. Briefly, 100 mL of the known Cr(VI) solution and a known quantity of adsorbents were combined over time in a shaker operating at 200 rpm. The adsorption experiments were investigated at a pH range of 1.0–12.0. To adjust the solution pH, 1 M NaOH/HNO_3 was used. The influencing variables were tested throughout the experiment at 25 ± 1 °C and 200 rpm shaking speed using a thermostatic shaker with a contact time (5–120 min), starting Cr(VI) concentration (10–200 ppm), and adsorbent mass (0.1–1.0 g). After adsorption experiments, Cr(VI) concentrations were analyzed spectrophotometrically following the Diphenyl Carbazide procedure at a wavelength of 540 nm using UV-Vis.[40] The difference between Cr(VI) removed and Cr(VI) remaining in the solution was used to calculate the quantity of Cr(VI) removal.

Equations (2) and (3) below were used to determine the removal capacity at any time (q_t) and equilibrium (q_e) (mg/g).

$$q_t = \frac{(C_o - C_t)V}{m} \tag{2}$$

$$q_e = \frac{(C_o - C_e)V}{m} \tag{3}$$

The adsorbent removal efficiency was calculated using Eq. (4)

$$\%\ RE = \frac{(C_o - C_e)}{C_o} * 100\% \tag{4}$$

where V- is the working solution volume (L), C_o and C_t-represent the starting concentration and concentration at any time (t) in (mg/L), m- is the mass of adsorbent, (g), and C_e-is the concentration at equilibrium.

Data analysis

The kinetics of the experimental data was evaluated using linear kinetic models, namely, Lagrangian pseudo-first-order (PFO) kinetic (Eq. 5), Pseudo-second-order (PSO) kinetic (Eq. 6), Elovich kinetic model (Eq. 7), and Intraparticle diffusion model (Eq. 8) as summarized in Table 1 below.

Regeneration of the adsorbents

To evaluate the regeneration capability of the functionalized cellulose nanocomposite, adsorption-desorption cycles were performed. After the initial adsorption of Cr(VI), the used adsorbent was separated from the solution and washed with deionized water to remove loosely bound ions. The adsorbent was then treated with deionized water, 0.1 M HCl and 0.1 M NaOH, separately and stirred for 1 h to release the adsorbed Cr(VI) ions. The desorbed Cr(VI) was quantified, and the adsorbent was thoroughly rinsed with deionized water until neutral pH was achieved. The regenerated adsorbent was dried at 60 °C in an oven and reused in a new batch of Cr(VI) solution under the same conditions as the initial adsorption experiment. This process was repeated for multiple cycles to assess the stability and reusability of the adsorbent. The adsorption efficiency after each regeneration cycle was calculated to determine the extent of performance retention over repeated uses.

Results and discussions

Functional group analysis (FTIR)

Figure 1a illustrates the FTIR spectra for the precursor materials (*Typha angustifolia*, CPC, and CNC), while Figure 1b show the spectra for Fe_3O_4NP, CNC-Fe_3O_4NP and CNC-Fe_3O_4NP-CD nanocomposites. From Figure 1a, the broad peak at around 3309 cm^{-1} is linked to intramolecular hydrogen bond O–H stretching, and the peaks at around 2892 and 2915 cm^{-1} are linked to C–H stretching of the cellulosic materials.[41] The wavenumber around 898 cm^{-1} is attributed to the C–H rocking vibration of cellulose. The peak at 1730 cm^{-1} was only observed in the *Typha angustifolia* grass powder due to the esters and acids only present in the lignin. Similarly, the bands at 1034 cm^{-1}, 1730 cm^{-1} and 1632 cm^{-1} are due to C–O–C of the pyranose ring, carboxyl groups found in esters and acids that are primarily found in lignin and O–H bending vibrations, respectively [42,43]. The peak was not seen in CPC and CNC samples, which is a clear indication that the esters and acids were successfully removed. At around 1157 cm^{-1}, a peak of O–H associated with C–O–H was present and was more extensive and more well-defined in cellulose than the rest of the samples, indicating a purer sample.[42] The O–H peak associated with absorbed water at around 1632 cm^{-1} was constant for all the samples.

The FTIR spectra for Fe_3O_4NP, CNC-Fe_3O_4NP and CNC-Fe_3O_4NP-CD are shown in Figure 1b. The spectrum for Fe_3O_4NP exhibited a significant band at 546 cm^{-1}, corresponding to the Fe–O stretching vibrations. This band confirmed the presence of magnetic Fe_3O_4NP within the

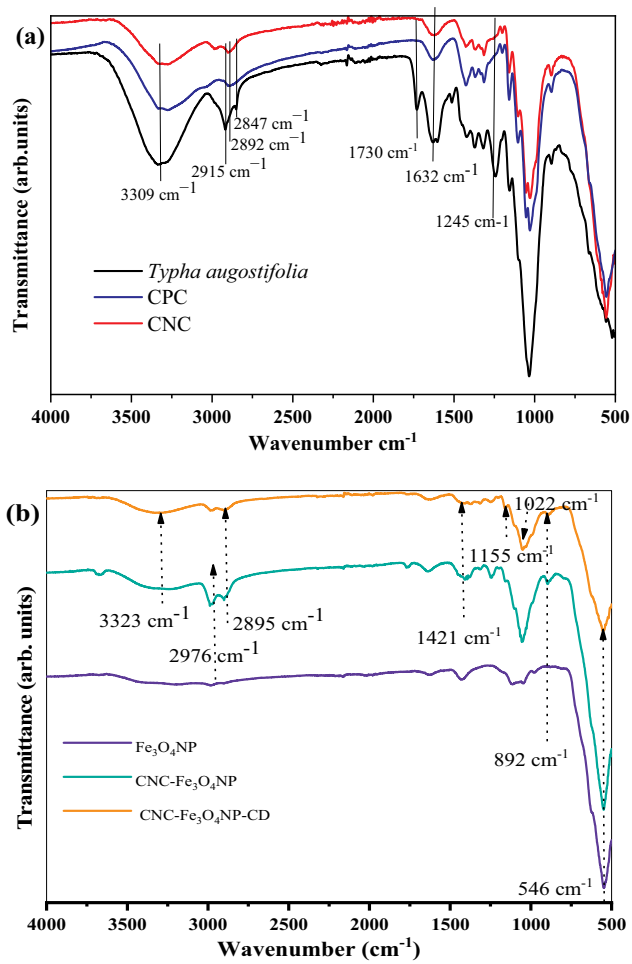

Figure 1. (a) FTIR spectra for *Typha angustifolia*, CPC, and CNC; (b) Fe_3O_4NP, CNC-Fe_3O_4NP and CNC-Fe_3O_4NP-CD nanocomposites.

Table 1. Kinetic Models.

Kinetic model	Non-linear equation	Linearised form	Plots	Eqs.
Pseudo first order	$\frac{dq_t}{dt} = K_1(q_e - q_t)$	$ln(q_e - q_t) = lnq_e - K_1 t$	$(q_e - q_t) vs\ t$	(5)
Pseudo second order	$\frac{dq_t}{dt} = K_2(q_e - q_t)^2$	$\frac{t}{q_t} = \frac{1}{K_2 q_e^2} + \frac{t}{q_e}$	$\frac{t}{q_t} vs\ t$	(6)
Elovich	$q_t = \beta lnt + \beta ln\alpha)$	$q_t = \frac{1}{\beta}\ln(1 + \alpha\beta t)$	$q_t\ vs\ lnt$	(7)
Intraparticle diffusion	$q_t = K_{id} t^{1/2}$	$q_t = K_{id} t^{1/2} + C$	q_t vs $t^{1/2}$	(8)

* K_1 is the PFO rate constant, K_2 is the PSO rate constant (g/mg.m); α (mg.g^{-1}min^{-1}) is the rate of chemisorption at zero coverage; β (g.mg^{-1}) is the Elovich desorption constant; $t^{1/2}$ is the square root of time (min$^{0.5}$) and K_{id} is the Intraparticle diffusion coefficient (mg/g.min$^{0.5}$).

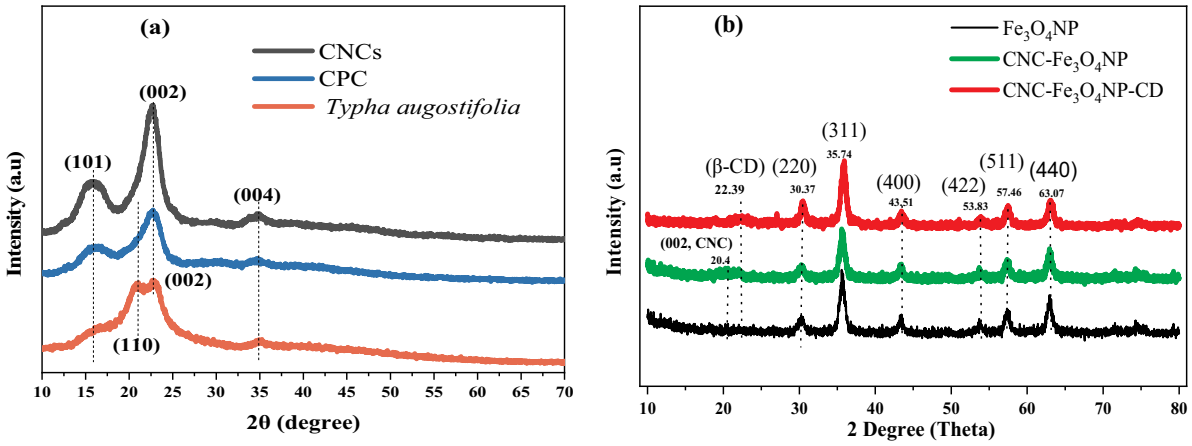

Figure 2. (a) XRD pattern for *Typha angustifolia*, CPC, and CNC; (b) Fe_3O_4NP, CNC-Fe_3O_4NP nanocomposites.

nanocomposites.[44] Additionally, the spectrum of CNC-Fe_3O_4NP and CNC-Fe_3O_4NP-CD nanocomposites showed peaks around 1421 cm^{-1} and 892 cm^{-1}, associated with the cellulose structure, indicating that the cellulose backbone remained intact after nanoparticle incorporation.[45] In addition, the peaks at around 3323 cm^{-1} are linked to intramolecular hydrogen bond O−H stretching. The peaks around 2895 and 2976 cm^{-1} represent the C−H stretching of the cellulosic materials, with only minor shifts and variations in intensity compared with that of CNCs. When functionalized with β-cyclodextrin (CD), the FTIR spectrum of CNC-Fe_3O_4NP-CD displays new peaks at 1022 cm^{-1} and 1155 cm^{-1}, corresponding to C−O−C and C−H bending vibrations from CD.[46] These additional peaks confirm the successful attachment of β-cyclodextrin to the CNC-Fe_3O_4NP nanocomposite. The inclusion of CD enhances the nanocomposite's capability to form host-guest complexes with various pollutants, improving its adsorption efficiency for hexavalent chromium (Cr(VI)).[47]

Crystalline structure analysis X-ray diffraction (XRD) analysis

Figure 2a shows the XRD patterns for the precursor materials (*Typha angustifolia*, CPC, and CNC), while Figure 2b show the spectra for Fe_3O_4NP, CNC- Fe_3O_4NP and CNC-Fe_3O_4NP-CD nanocomposites. From Figure 2a, the (101) crystalline planes correspond to hemicellulose,[48] while the (002) planes correspond to the monoclinic structure of cellulose I.[49] Similarly, the third XRD reflex, which appears as a blurred band, confirms the presence of the (040) crystal phases from the amorphous regions (primarily lignin and hemicellulose). It is reported that for cellulose I and II, the 2θ peak intensity values of crystal cellulose are linked to 22.5° and 20.1°, respectively. The highest intensity value of amorphous cellulose is located at 18° for cellulose I and 16.3° for cellulose II.[50] The CNC peak pattern at 22.64° corresponds to the crystalline cellulose I structure, while the amorphous cellulose II corresponds to 2θ at 15.83°. For CPC, crystalline cellulose II and crystalline cellulose I show peak intensity values at 16.23° and 22.58°, respectively. The powdered *Typha angustifolia* showed peaks with intensity values of 2θ of 16.11°, 21.00°, and 22.89° representing amorphous cellulose I, amorphous cellulose II, and crystalline cellulose II.[50,51]

From Figure 2b, the XRD patterns of CNC-Fe_3O_4NP exhibit peaks corresponding to cellulose and Fe_3O_4, confirming the presence of magnetic nanoparticles. The distinct peaks at 2θ values of around 30.0°, 35.4°, 43.2°, 57.0°, and 62.7° correspond to the (220), (311), (400), (422), (511), and (440) reflections of Fe_3O_4, respectively.[52] The functionalization with β-cyclodextrin resulted in XRD patterns that show additional broad reflection profiles centered at 22.5°, attributed to the amorphous nature of CD. These results indicate that the crystalline structure of the Fe_3O_4NP is retained while introducing the amorphous CD, enhancing the nanocomposite's functionality for Cr(VI) adsorption. These XRD findings are consistent with the research by Ding et al.[53], who highlighted the importance of XRD in verifying the crystalline phases of incorporated nanoparticles. The presence of crystalline and amorphous components ensures a balance between structural features and functional flexibility, which might enhance CNC-Fe_3O_4NP-CD removal efficiency for Cr(VI).

Scanning electron microscopy (SEM) analysis

Figure 3(a–c) presents SEM images showing the surface morphology of Fe_3O_4NP, CNC-Fe_3O_4NP, and CNC-Fe_3O_4NP-CD nanocomposites. The SEM analysis provides crucial insights into the structure and distribution of the components within these materials. In the case of Fe_3O_4NP (Figure 3a), the image reveals the presence of large aggregates, which are common due to the magnetic nature of Fe_3O_4, which causes its particles to attract each other and form clusters. This agglomeration can reduce the surface area available for adsorption, potentially limiting the efficiency of the nanoparticles in adsorbing contaminants like chromium (Cr(VI)) from aqueous solutions.[54] For the CNC-Fe_3O_4NP nanocomposites (Figure 3b), the SEM images display a significant reduction in agglomeration, with the particles forming more uniform and attached to the CNCs rod-like structures. Introducing cellulose nanocrystals (CNCs) appears to help disperse the Fe_3O_4NP more evenly. CNCs, naturally fibrous and possessing abundant hydroxyl groups, interact with the nanoparticles, providing a

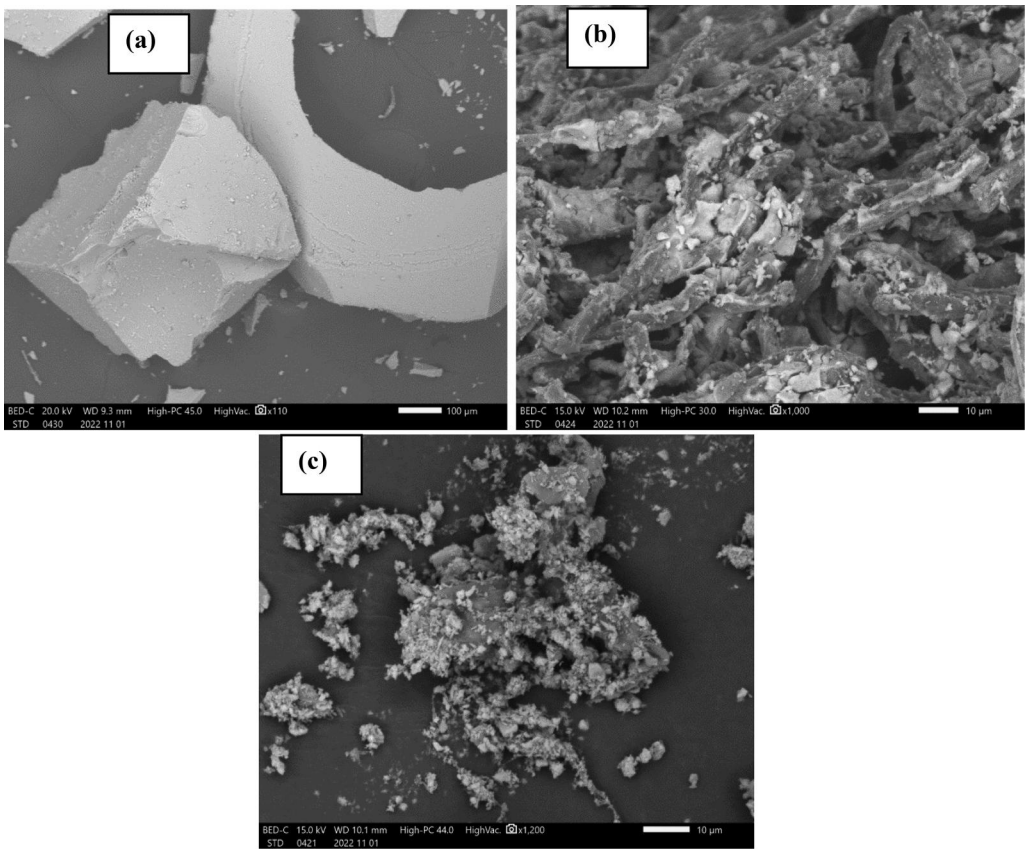

Figure 3. SEM images for Fe_3O_4NP, CNC-Fe_3O_4NP, and CNC-Fe_3O_4NP-CD nanocomposites.

steric hindrance that mitigates their tendency to clump together.[55] The improved dispersion increases the surface area and exposes more active sites, enhancing the material's adsorption capacity.[55]

The further modification to CNC-Fe_3O_4NP-CD (Figure 3c) shows an even more homogeneous dispersion without significant agglomeration like the one for the Fe_3O_4NP. The presence of β-cyclodextrin appears to enhance this dispersion further. β-CDs' unique toroidal structure and the ability to form inclusion complexes likely contributed to the stabilization of the nanoparticles, preventing them from agglomeration. The uniform distribution observed in these nanocomposites indicates a higher availability of active sites, which can enhance the efficiency of Cr(VI) adsorption. The presence of β-CD also provided additional functional groups that can interact with Cr(VI), potentially increasing this contaminant's adsorption capacity and selectivity.[56]

The enhanced dispersion and reduced agglomeration observed in CNC-Fe_3O_4NP and CNC-Fe_3O_4NP-CD suggest an increased surface area and uniform distribution of active sites for effective adsorption of metal ions. Similar results were reported by Marcelo et al.[56], and Zhao et al.[57], who found that there was an improvement in the adsorption capacity of nanocomposites incorporated stabilizers and dispersion agents.

Energy Dispersive Spectroscopy (EDS)

EDS was further employed to confirm the elemental composition of Fe_3O_4NP, CNC-Fe_3O_4NP, and CNC-Fe_3O_4NP-CD nanocomposites (Figure 4a–c). The data reveal significant changes in the elemental composition with the addition of Fe_3O_4 and β-cyclodextrin to cellulose nanocrystals. The EDS analysis of Fe_3O_4NP showed the predominant presence of iron (Fe), carbon (C) and oxygen (O) with mass percentages of 70.41%, 17.81% and 11.77%, respectively (Figure 4a). The high concentration of iron is due to Fe_3O_4, primarily composed of iron oxide. The carbon (C) content is relatively low, indicating minimal contamination or the presence of organic material in the sample [58]. The atom percentages reflect a similar distribution, with iron being the dominant component. As seen in Figure 4b, the EDS data reveal an increase in the C content, indicated by a mass percentage of 25.32%. This increase in carbon content is attributed to the organic nature of CNCs. The O content also increased slightly (36.75%), which can be associated with the CNCs and the Fe_3O_4NP. Notably, the Fe content decreased to 37.70%, reflecting the partial coating of the nanoparticles with CNCs, which is consistent with the reduction in the surface density of iron due to the presence of the organic CNC matrix.[59]

Further functionalization with β-cyclodextrin to form CNC-Fe_3O_4NP-CD (Figure 4c) showed a slight increase in carbon content to 39.78%, highlighting the organic nature of β-cyclodextrin. Oxygen content also increased to 36.75%, likely due to the abundant hydroxyl groups in CNCs and β-CD. The iron content decreased further to 21.90%, which could be attributed to the introduction of β-cyclodextrin, which contributed more organic material, reducing the relative amount of iron detected. The changes in the elemental

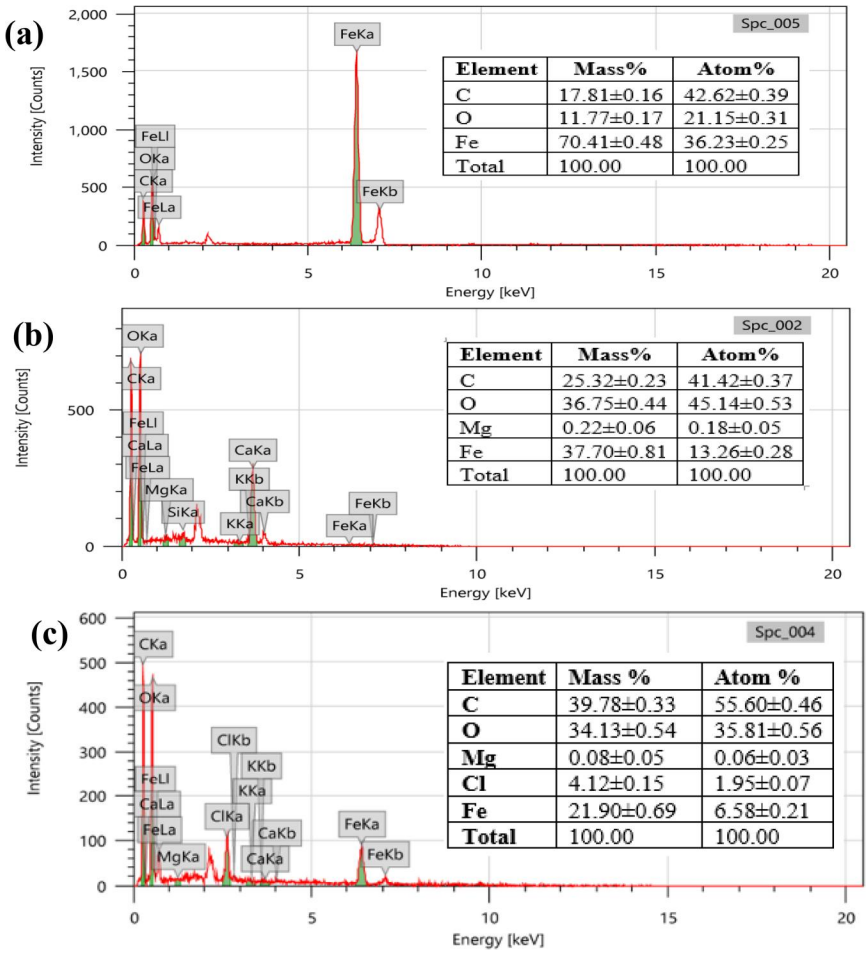

Figure 4. EDS data for (a). Fe_3O_4NP, (b). CNC-Fe_3O_4NP and (c). CNC-Fe_3O_4NP-CD nanocomposites.

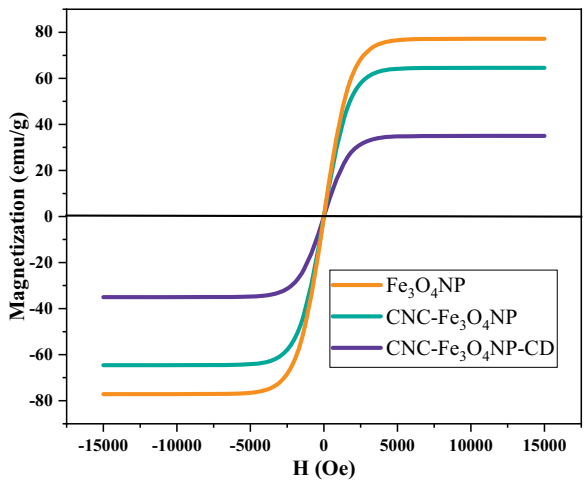

Figure 5. VSM for Fe_3O_4NP, CNC-Fe_3O_4NP, and CNC-Fe_3O_4NP-CD nanocomposites.

composition suggested successful incorporation of Fe_3O_4NP, β-CD, and CNCs in the nanocomposite adsorbent.

Vibrating sample magnetometer (VSM) analysis

The hysteresis loops in Figure 5 reveal significant insights into the magnetic behavior of Fe_3O_4NP, CNC-Fe_3O_4NP and CNC-Fe_3O_4NP-CD, confirming their superparamagnetic nature. The VSM data indicates that pure Fe_3O_4NP exhibits high magnetization values of 77.14239 emu/g at an applied magnetic field (H) of ±15,000 Oe. This high magnetization is expected for Fe_3O_4NP due to their strong magnetic properties. The coercivity and remanence values are close to zero, indicating superparamagnetic behavior. This is advantageous for applications requiring quick magnetic response and easy re-dispersion once the external magnetic field is removed. A slight reduction in magnetization is observed upon incorporating Fe_3O_4NP into cellulose nanocrystals to form CNC-Fe_3O_4NP. The magnetization value decreases to 64.56152 emu/g at the same applied field of ±15,000 Oe. This reduction can be attributed to the dilution of magnetic Fe_3O_4 content by the non-magnetic CNC matrix. However, the composite retained a significant portion of its magnetic properties, which is substantial for targeted adsorption and separation in wastewater treatment processes.

Further functionalization with β-cyclodextrin to form CNC-Fe_3O_4NP-CD resulted in a further reduction in magnetization, with values reaching 34.97082 emu/g at ±15,000 Oe. The additional layer of β-cyclodextrin could have contributed to this decrease, as it introduces more non-magnetic material into the composite.[60] Despite this reduction, the CNC-Fe_3O_4NP-CD nanocomposite remained superparamagnetic, as evidenced by the low coercivity and remanence values. This superparamagnetic property ensures

the composite can respond quickly to an external magnetic field and be easily separated from aqueous Cr(VI) solutions.

Batch adsorption studies

Effect of pH on removal of Cr(VI)

Figure 6 shows the removal efficiency of Cr(VI) metal ions using CPC, CNC, CNC-Fe_3O_4NP, and CNC-Fe_3O_4NP-CD adsorbents across pH 1 to 12. The findings reveal a significant influence of pH on adsorption efficiency owing to the metal ion's pH-dependent behavior. At pH 1, the removal efficiencies are 60.21%, 68.45%, 80.45%, and 94.45% for CPC, CNC, CNC-Fe_3O_4NP and CNC-Fe_3O_4NP-CD, respectively. At pH 2, removal efficiency is seen to increase for all adsorbents, with CNC-Fe_3O_4NP-CD reaching 97.45%, which could be attributed to the optimal balance between the positively charged adsorbent sites and Cr(VI) metal ion species. The observed significant efficiency at low pH could be attributed to protonation, which increases the positive charge on the adsorbent surface, enhancing electrostatic attraction with negatively charged Cr(VI) species ($HCrO_4^-$ and $Cr_2O_7^-$).[61] Furthermore, the improved removal efficiency in CNC-Fe_3O_4NP nanocomposite could be attributed to iron oxide nanoparticles, which provided more active sites, while CNC-Fe_3O_4NP-CD's superior performance is due to β-cyclodextrin's ability to form inclusion complexes with Cr(VI) ions. However, as the pH was increased from 3 to 4, a slight decline in removal efficiency was observed, which can be attributed to reduced H^+ availability and positive charge density on the adsorbent surface.[61] At pH 4, the removal efficiency was found to be 55.25%, 60.65%, 88.98%, and 90.12% for CPC, CNC, CNC-Fe_3O_4NP and CNC-Fe_3O_4NP-CD, respectively. This decline is more pronounced for CPC and CNC due to their lower ability to maintain a positive charge than the modified nanocomposites. At pH 5 and above, removal efficiencies further declined, with CNC-Fe_3O_4NP-CD maintaining a relatively high efficiency of 64.78% even at pH 12, suggesting enhanced resistance to pH changes.

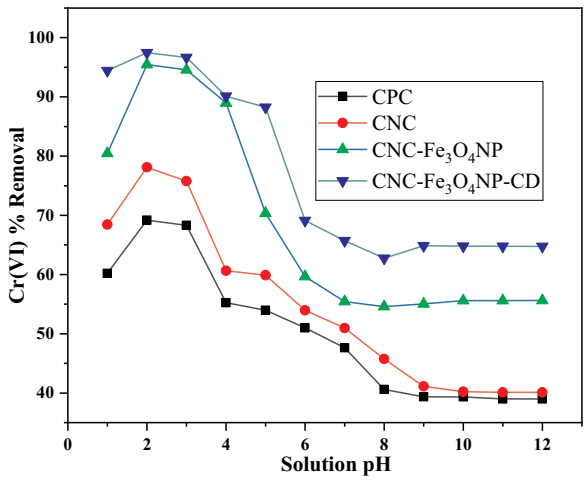

Figure 6. The influence of pH on the removal of Cr(VI) using different adsorbents.

According to Li et al.,[62] bulk metal ions occur in aqueous solutions with a pH range of 2.0-8.5 as $M^{+/2+}$ or $M(OH)^+$ ions. The majority of metal ions precipitate because they create $M(OH)^{2+}$ above this pH (basic character of the solution). Thus, it is usually safe to do adsorption tests below pH 9.0 in order to avoid metal ion precipitation. Similarly, at very low pH levels, the concentration of H_3O^+ ions is significantly greater and surpasses that of metal ions. The overabundance of H_3O^+ ions surrounds the adsorbent's active sites, permitting unhindered metal ion mobility in the solution.[63] This results in competing reactions involving the H_3O^+ ions of the adsorbate metal ions. Positively charged metal ions adhere to the accessible binding sites on the adsorbent when the solution's pH rises due to less competition.[64,65]

Based on several adsorption processes, the adsorption of hexavalent chromium (Cr(VI)) by CNC-Fe_3O_4NP-CD nanocomposite adsorbent may be explained by the following reaction mechanisms: complexation, reduction, electrostatic attraction, and host-guest interactions with β-cyclodextrin (CD) as shown in Eqs. (9–13).[61,66–71]

$$\text{CNC-Fe}_3\text{O}_4\text{NP-CD}+_{(s)} + \text{HCrO}_4^- \text{ (aq)} \rightarrow \text{CNC-Fe}_3\text{O}_4\text{NP-CD-HCrO}_{4\,(s)}^- \text{ (Electrostatic attraction)} \quad (9)$$

$$3\text{Fe}^{2+}{}_{(aq)} + \text{CrO}_4^{2-}{}_{(aq)} + 8\text{H}^+{}_{(aq)} \quad 3\text{Fe}^{3+}{}_{(aq)} + \text{Cr}^{3+}{}_{(aq)} + 4\text{H}_2\text{O}_{(l)} \text{ (Reduction)} \quad (10)$$

$$\text{CNC-OH}_{(s)} + \text{CrO}_4^{2-}{}_{(aq)} \rightarrow \text{CNC-O-CrO}_4^{2-}{}_{(s)} \text{ (Complexation)} \quad (11)$$

$$\text{Fe-OH}_{(s)} + \text{CrO}_4^{2-}{}_{(aq)} \rightarrow \text{Fe-O-CrO}_4^{2-}{}_{(s)} \text{ (Complexation)} \quad (12)$$

$$\text{CD}_{(s)} + \text{HCrO}_{4\,(aq)}^- \rightarrow \text{CD-HCrO}_{4\,(s)}^-$$
$$\text{(Host-Guest interaction via } \beta\text{-Cyclodextrin)} \quad (13)$$

Adsorbent mass on the removal of Cr(VI)

The influence of adsorbent mass on Cr(VI) removal was studied by varying the mass of CPC, CNC, CNC-Fe_3O_4NP, and CNC-Fe_3O_4NP-CD adsorbents from 0.2 g to 1.4 g, with other parameters constant. The results showed an overall increase in removal efficiency with higher adsorbent mass for all materials (Figure 7). At a low adsorbent mass of 0.2 g, removal efficiencies were relatively low: 16.45% for cellulose, 18.43% for CNC, 27.94% for CNC-Fe_3O_4NP, and 35.67% for CNC-Fe_3O_4NP-CD. This low efficiency could be attributed to the limited active sites available for adsorption. As the adsorbent mass increased to 0.4 g and 0.6 g, the removal efficiency improved significantly, particularly for CNC-Fe_3O_4NP-CD, reaching 49.7% and 68.45%, respectively. This improvement could be attributed to increased adsorption sites, with the Fe_3O_4NP and β-cyclodextrin providing additional surface area and functional groups. At 0.8 g, CNC-Fe_3O_4NP-CD achieved nearly complete removal

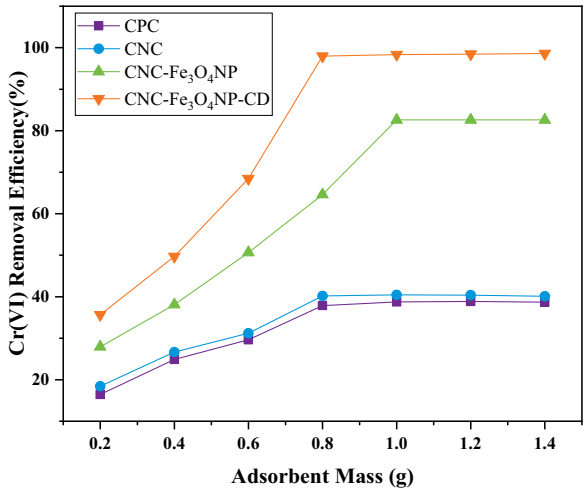

Figure 7. The influence of adsorbent mass on the removal of hexavalent chromium.

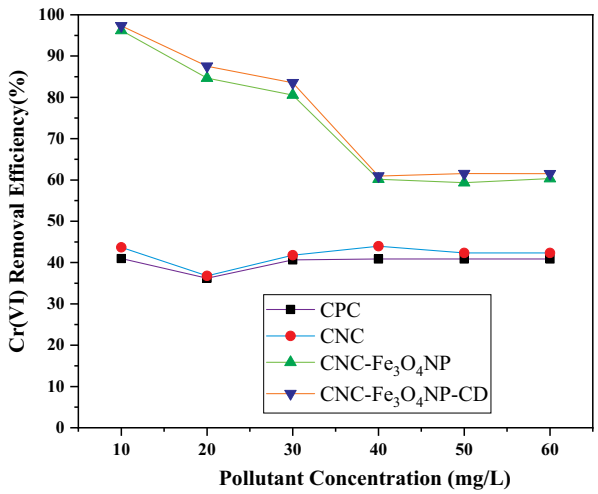

Figure 8. The influence of Cr(VI) concentration on adsorption using different adsorbents.

with 97.98% efficiency, and CNC-Fe_3O_4NP showed a significant increase to 64.61%. This suggests that active site availability was not yet limited to the adsorption process. Cellulose and CNC also improved, with maximum removal efficiencies of 37.87% and 40.19%, reflecting their lower surface area and active site availability. At 1.0 g, the maximum removal efficiencies were observed: 98.34% for CNC-Fe_3O_4NP-CD, 82.62% for CNC-Fe_3O_4NP, 40.44% for CNC, and 38.76% for CPC. This indicates that at this dosage, particularly for CNC-Fe_3O_4NP and CNC-Fe_3O_4NP-CD, sufficient active sites were available to adsorb nearly all Cr(VI) ions. Beyond 1.0 g, 1.2 g and 1.4 g, the increase in removal efficiency plateaued, especially for CNC-Fe_3O_4NP and CNC-Fe_3O_4NP-CD. CNC-Fe_3O_4NP-CD showed a slight increase from 98.45% at 1.2 g to 98.61% at 1.4 g, indicating that the adsorption reached equilibrium, where additional adsorbent did not significantly enhance efficiency due to saturation of active sites.

From the findings, CNC-Fe_3O_4NP-CD was the most effective adsorbent, achieving the highest removal efficiency across all dosages. Its superior performance is due to enhanced surface area, magnetic properties, and β-cyclodextrin, which provided additional binding mechanisms for Cr(VI) ions, increasing adsorption site accessibility and efficiency

Varying pollutant concentration

The influence of initial Cr(VI) concentration on the removal of Cr(VI) ions was evaluated using CPC, CNC, CNC-Fe_3O_4NP, and CNC-Fe_3O_4NP-CD in mimicked wastewater, with concentrations ranging from 10-60 mg/L (Figure 8). From the findings, at the lowest Cr(VI) concentration (10 mg/L), all adsorbents showed significant removal efficiencies, with CNC-Fe_3O_4NP and CNC-Fe_3O_4NP-CD achieving 97.21% and 97.31%, respectively. This significant adsorption efficiency could be attributed to the ample availability of active sites relative to the Cr(VI) ions present, allowing effective adsorption. As the concentration of Cr(VI) ions increased to 20 mg/L, removal efficiency declined across all adsorbents. CNC-Fe_3O_4NP-CD maintained a relatively high efficiency of 87.56%, while CNC-Fe_3O_4NP achieved 84.67%. At 30 mg/L, removal efficiencies continued to drop, reaching 80.57% for CNC-Fe_3O_4NP and 83.54% for CNC-Fe_3O_4NP-CD, indicating that active sites were nearing full occupancy and competition for these sites is intensified. Further increases in concentration to 40 mg/L and beyond led to more significant declines in the removal efficiency. At 60 mg/L, CNC-Fe_3O_4NP and CNC-Fe_3O_4NP-CD exhibited similar efficiencies of approximately 60.32% and 61.53%, respectively, indicating that the adsorbents had reached saturation and could not effectively adsorb additional Cr(VI) ions. In contrast, CNC maintained lower but stable removal efficiencies of around 40% across all concentrations.

CNC-Fe_3O_4NP-CD nanocomposite adsorbent consistently outperformed other adsorbents, especially at lower concentrations, due to its enhanced surface area, higher number of active sites, and better dispersibility caused by Fe_3O_4NP and β-CD. The decline in efficiency with increasing Cr(VI) concentration offers a significant advantage over maintaining high adsorption capacity under high pollutant concentrations, which is critical for practical wastewater treatment applications.

Varying adsorption contact duration

The influence of contact time on Cr(VI) removal efficiency was studied over 1-35 min (Figure 9). Initially, at the first minute, slight adsorption occurred, with CNC-Fe_3O_4NP-CD showing the highest removal efficiency (10.56%), followed by CNC-Fe_3O_4NP (10.23%), CNC (6.7%), and CPC (2%). This rapid initial adsorption is due to the abundant active sites on the adsorbents. After 5 min, removal efficiencies increased significantly, with CNC-Fe_3O_4NP-CD reaching 40.56%, CNC-Fe_3O_4NP (31.98%), CNC (17.99%), and CPC (15%). By 10 min, CNC-Fe_3O_4NP-CD attained 60.89% removal efficiency, CNC-Fe_3O_4NP (50.56%), CNC (20.55%), and CPC (18%), indicating that adsorption was progressing toward equilibrium. From 15 to 20 min, CNC-Fe_3O_4NP-CD

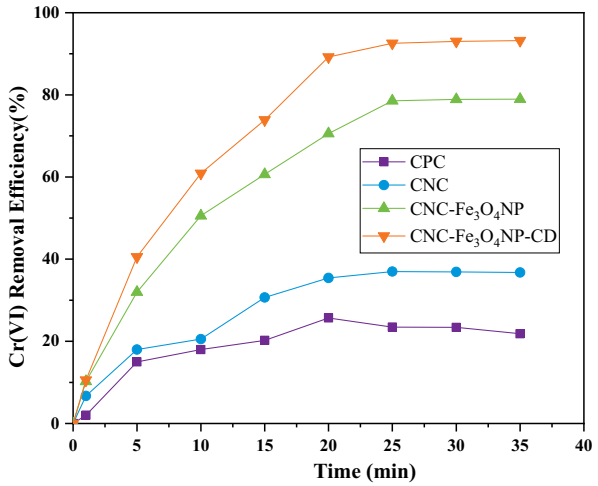

Figure 9. The influence of contact time on the removal of Cr(VI) using different adsorbents.

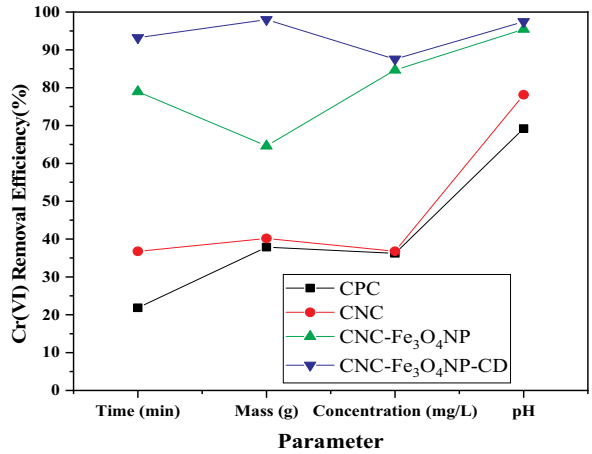

Figure 10. Comparative study of the adsorbents at pH 2, Cr(VI) 20 mg/L, adsorbent mass of 1 g/L, Contact time of 35 min at room temperature.

and CNC-Fe_3O_4NP exhibited substantial increases in efficiency, reaching 89.23% and 70.56%, respectively, while CNC and CPC increased more gradually. By 25 min, CNC-Fe_3O_4NP-CD attained 92.56% removal efficiency and CNC-Fe_3O_4NP 78.56%, with CNC and CPC recording lower efficiencies of 36.98% and 23.45%. Within 30 min, the adsorption for CNC-Fe_3O_4NP-CD and CNC-Fe_3O_4NP plateaued, recording 93.01% and 78.88% removal efficiency. At 35 min, CNC-Fe_3O_4NP-CD and CNC-Fe_3O_4NP attained 93.2% and 78.95%, while CNC and CPC reached equilibrium with lower efficiencies. The results highlight the superior performance of CNC-Fe_3O_4NP-CD, attributed to its enhanced surface area and active site availability, which facilitate rapid and effective Cr(VI) adsorption.

These findings suggest that the contact time significantly influences the adsorption efficiency, with optimal adsorption occurring within the first 20 min for CNC-Fe_3O_4NP-CD. For practical applications, this implies that using CNC-Fe_3O_4NP-CD can achieve efficient removal of Cr(VI) in a relatively short contact time, making it an effective adsorbent for rapid water treatment processes.

Comparative study on the adsorbents

The effectiveness of CPC, CNC, CNC-Fe_3O_4NP, and CNC-Fe_3O_4NP-CD adsorbents toward the removal of Cr(VI) from mimicked aqueous media was assessed under a range of influencing parameters, including temperature, pH, adsorbent dose, pollutant concentration, and contact time (Figure 10). From the findings of the study; the results consistently demonstrated the superior performance of CNC-Fe_3O_4NP-CD, particularly at low pH levels, which is critical for efficient Cr(VI) removal, which can be attributed to the positive charge on the adsorbent surface that enhances electrostatic attraction with negatively charged Cr(VI) ions. The incorporation of Fe_3O_4NP and β-cyclodextrin in CNC-Fe_3O_4NP-CD not only increased the surface area and provided additional active sites for adsorption but also enhanced the material's stability and dispersibility, leading to higher removal efficiencies compared to the other adsorbents.

Regarding adsorbent dosage, CNC-Fe_3O_4NP-CD achieved nearly complete removal at lower masses, indicating a higher number of accessible active sites and efficient binding mechanisms, further supported by the functional groups present as evidenced by FTIR analysis. At varying initial Cr(VI) concentrations, CNC-Fe_3O_4NP-CD maintained high removal efficiencies, particularly at lower concentrations, demonstrating its capacity to effectively adsorb Cr(VI) even as the pollutant concentration increases. The study also highlighted the rapid adsorption kinetics of CNC-Fe_3O_4NP-CD, reaching equilibrium quickly, which is advantageous for practical water treatment applications where time efficiency is crucial.

Given these findings, CNC-Fe_3O_4NP-CD is this study's most effective adsorbent for Cr(VI) removal, offering high efficiency, rapid kinetics, and stability across various conditions. Its unique composition, combining the benefits of cellulose nanocrystals, Fe_3O_4NP, and β-cyclodextrin, provides multiple interaction mechanisms, making it ideal for kinetic studies. CNC-Fe_3O_4NP-CD was, therefore, chosen for kinetics studies.

Table 2 provides several materials and methods related to adsorption toward hexavalent chromium removal for water/aqua medium using cellulose-based and iron oxide nanoparticle adsorbents. According to the listed investigations in Table 2, the current study's adsorbent showed excellent sorption efficiency comparable to other research work. As a result, it has a boundless potential for optimization and application in acidic wastewater purification.

Kinetics studies of adsorption

Pseudo-first-order kinetic models

To investigate the kinetic behavior and mechanism of Cr(VI) adsorption onto the CNC-Fe_3O_4NP-CD nanocomposite adsorbent, the linear regression coefficient (R^2) was used to demonstrate the applicability of the pseudo-first-order kinetic model across several experimental data sets. The study findings are provided in Figure 11 and Table 3

The results led to relatively low linear regression coefficients (R^2) ranging from 0.55538 to 0.94783. This indicates that the model was inappropriate, given the current

Table 2. Several materials and methods related to the adsorption of Cr(VI).

Adsorbent	% Removal efficiency	Reference
CNC-Fe_3O_4NP-CD	97.45%	Current work
Polypyrrole magnetic nanocomposite	99.2%	[72]
Sodium carboxymethyl cellulose stabilized zerovalent iron nanoparticles	88.5%	[73]
Iron Oxide Particles	82%	[74]
Cellulose Nanocrystal–Magnetic Iron Oxide Nanocomposite	91.78%	[65]
Cellulose biochar supported iron nanoparticles	97.23%	[75]
Chitosan-coated superparamagnetic iron oxide nanoparticles	>92%	[76]
Stabilized iron sulfide nanoparticles	82.23%	[77]
Bio-based iron oxide nanoparticles	98.71%	[78]
Carboxymethyl Cellulose–Stabilized Sulfidated Nano Zerovalent Iron	85.08%	[79]

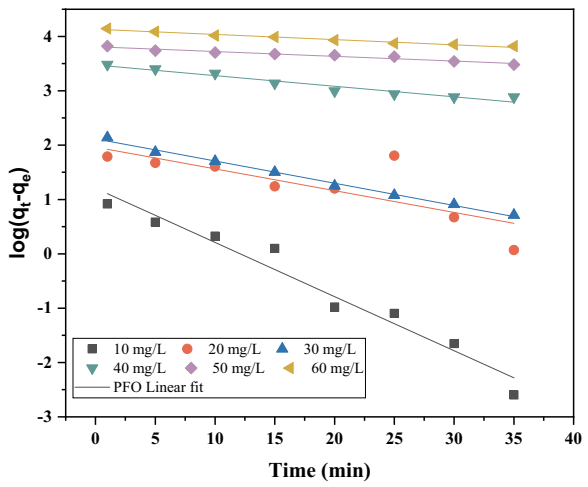

Figure 11. Pseudo-first-order kinetic model linear fit.

Table 3. Summary of kinetic model parameters.

	Parameters				
Kinetic model/ Adsorbate	10 mg/L	20 mg/L	30 mg/L	40 mg/L	60 mg/L
Pseudo-first kinetic model					
qe (exp)(mg/g)	4.361	8.426	16.412	28.983	35.509
qe (model) (mg/g)	4.234	7.897	15.028	27.671	34.280
k_1(mg/g)	0.00814	0.01284	0.00127	0.00196	0.01205
R^2	0.91513	0.55538	0.93332	0.9333	0.94783
Pseudo second kinetic model					
qe (model) (mg/g)	4.154	7.3043	15.419	26.881	34.114
K_2(g/mg.min)	0.52803	0.29292	0.15689	0.10498	0.09251
R^2	0.9925	0.99747	0.98417	0.99781	0.98051
Elovich kinetic model					
α(mg/g.min)	0.19591	0.75835	0.42567	1.88423	1.52761
β(g/mg)	0.07228	0.27979	0.1101	0.15705	0.69519
R^2	0.93083	0.9362	0.95093	0.96044	0.93083
Intraparticle kinetic model					
Kid(mg/g.min$^{0.5}$)	0.50892	0.98097	0.5805	1.3161	3.39731
C	1.46329	1.99285	8.83463	10.15689	19.73795
R^2	0.98776	0.92505	0.99342	0.95541	0.98776

adsorption system on the CNC-Fe_3O_4NP-CD nanocomposite adsorbent. Furthermore, owing to the poor linear regression coefficient (R^2), the extremely low values of (q_{cal}) further confirm the model's failure.

Pseudo-second-order kinetic model

The findings on the applicability of the pseudo-second-order kinetic model for the study are presented in Figure 12 and Table 3. The experimental data under various physio-chemical conditions fitted well to the second-order kinetic linear model. The model displayed high linear regression coefficient values (R^2>0.98). This demonstrates that electron sharing between the solute and adsorbent occurred. Furthermore, lower values of the second-order kinetic constant K_2 were obtained because there was less competition between the metal ions and the adsorption site at the higher initial concentration. Numerous studies on the removal of heavy metals, including zinc (Zn^{2+}), copper (Cu^{2+}), and nickel (Ni^{2+}), demonstrated that these systems also followed pseudo-second-order kinetics.[80–82] These results imply that a single-step process governs Cr(VI) ion adsorption on the CNC-Fe_3O_4NP-CD nanocomposite adsorbent and entails several steps.[83]

Elovich model

The kinetics of chemisorption on heterogeneous adsorbents were quantified using the Elovich model. The model predicts

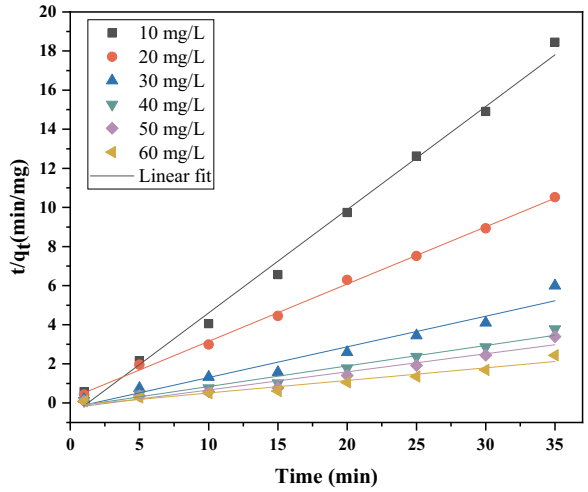

Figure 12. Pseudo-second-order kinetic model linear fit.

the existence of heterogeneous active surface sites with various activation energies.[84] Figure 13 and Table 3 illustrate how the model's linear fit to the experimental data allowed for the derivation of the Elovich constants and linear correlation coefficient. According to the Elovich model's adsorbent coefficient of determination, the adsorption of Cr(VI) onto the CNC-Fe_3O_4NP-CD nanocomposite adsorbent was chemically guided (R^2 > 0.93). Furthermore, the CNC-Fe_3O_4NP-CD nanocomposite adsorbent effectively adsorbed the metal ions owing to the initial sorption rates exceeding

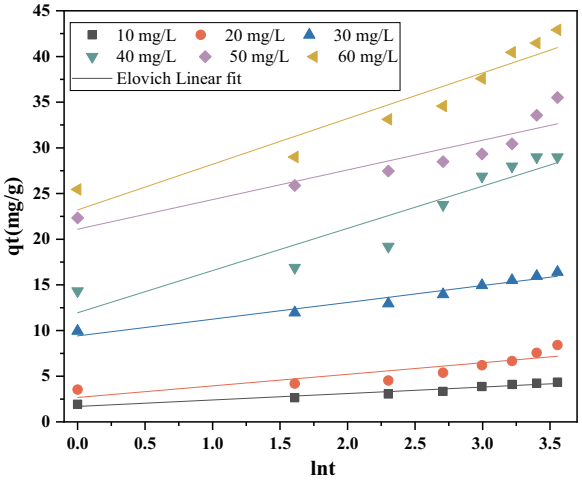

Figure 13. Elovich kinetic model linear fit.

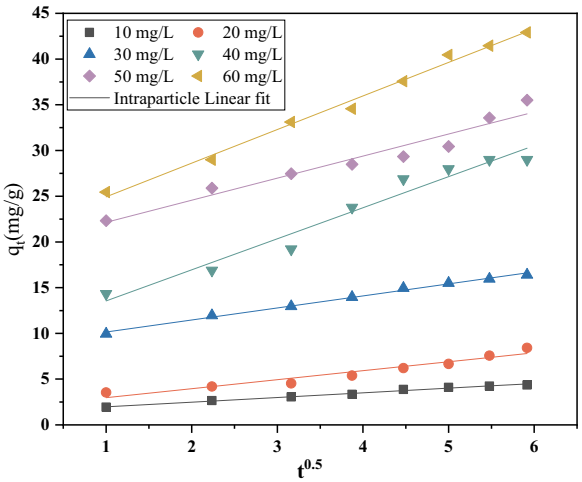

Figure 14. Intraparticle diffusion kinetic model linear fit.

their corresponding desorption constants.[85] In the Elovich model, active surface sites are assumed to be heterogeneous and to have a range of activation energies.[86]

Intra-particle diffusion model

The intraparticle diffusion model sometimes referred to as the Webber-Morris model, is crucial for understanding the behavior of any adsorption process.[80] Understanding the adsorption mechanism and how it underlies the system's apparent dynamic behavior is vital for designing and controlling any large-scale adsorption system. According to the results of this study, as shown in Figure 14 and Table 3, the Cr(VI) ions adsorb pretty quickly at first before slowing down. The rate-limiting step is frequently predicted using this model for an adsorption system involving porous materials. The model states that an entire system is controlled by intraparticle diffusion when the plot between qt and $t^{0.5}$ results in a straight line that goes through the origin. However, the plot in this study did not result in a single straight line passing through the origin. As a result of the observation, the adsorption mechanisms can be listed as metal ion transport from the bulk solution to the adsorbent

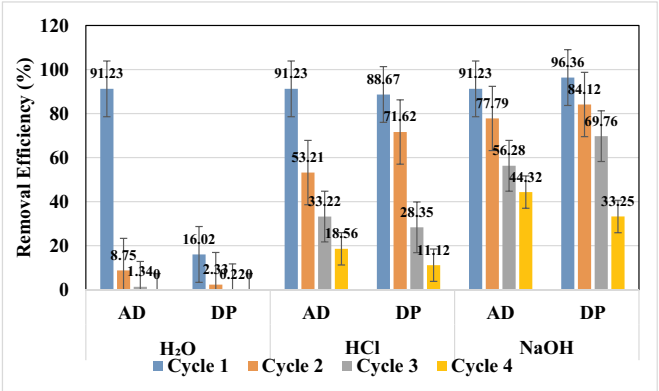

Figure 15. Regeneration of the adsorbent.

surface, diffusion across the adsorbent surface's boundary layer, adsorption on the adsorbent surface's active site and through intra-particle diffusion into the adsorbent's pores. The slowest step, external film diffusion, or pore diffusion, regulates the total adsorption rate.[87]

Regeneration of CNC-Fe_3O_4NP-CD

Figure 15 illustrates the regeneration efficiencies achieved using different eluents across multiple cycles. The regeneration of the CNC-Fe3O4NP-CD nanocomposite is a crucial aspect of its practical application in water treatment. Effective regeneration allows for multiple cycles of use, thereby reducing operational costs and enhancing sustainability. The regeneration process involved the desorption of adsorbed metal ions using deionized water, HCl, and NaOH as eluents.

From the findings of this study, the regeneration process's efficiency decreased with subsequent cycles due to potential surface modification or fouling of the adsorbent. Initially, HCl and NaOH achieved desorption efficiencies above 90%, but this efficiency declined with each cycle (Figure 15). NaOH provided the highest desorption efficiency over multiple cycles. The decrease in efficiency is likely due to changes in the surface chemistry of the CNC-Fe_3O_4NP-CD, such as the possible formation of insoluble complexes or the irreversible binding of some ions.

From the findings CNC-Fe_3O_4NP-CD nanocomposite exhibited good potential for reuse in multiple adsorption-desorption cycles, especially when using NaOH as an eluent. However, the gradual decline in efficiency suggests that periodic regeneration and potential chemical treatments may be necessary to maintain high performance. The adsorbents stability under various pH conditions and its ability to maintain significant adsorption capacity make it a promising sorbent for practical water treatment applications, where cost-effectiveness and sustainability are critical considerations.

Safe disposal of the Cr(VI)-loaded CNC-Fe_3O_4NP-CD nanocomposite adsorbent

Heavy metal ions loaded adsorbents disposal in the open air is not recommendable because of metal ions leaching. As a

result, the heavy metal ions-loaded CNC-Fe_3O_4NP-CD nanocomposite adsobent was incinerated at a temperature of 680-700 °C to produce ash, which was then mixed with 25 mL of deionized water to yield a liquid-solid ratio of 5:1.[88–90] After 24 h of continuous stirring, the metal ion concentration was determined using filtrates. It was found that Cr(VI) ions were found to be 0.00963 mg/L, which is way below the permissible limits (water ≈ 0.05 mg/L, soil ≈ 64 mg/kg, and air ≈ 5 μg/m^3) in the leach solutions.[91–93] However, Fe(II) was detected, which could be attributed to Fe_3O_4 nanoparticles. As a result, the ash is suitable for use as a catalyst in various industrial processes involving iron catalysts.

Conclusion

This research work successfully prepared and characterized a novel adsorbent of *β*-cyclodextrin capped magnetic nanoparticles anchored on cellulosic matrix (CNC-Fe_3O_4NP-CD) for the effective removal of hexavalent chromium (Cr(VI)) from synthetic wastewater. The work involved a multi-step process, including the extraction of cellulose from *Typhacaea angustifolia*, preparation of cellulose nanocrystals *via* acid hydrolysis, incorporation of Fe_3O_4NP, and functionalization with *β*-cyclodextrin through shear homogenization. Combining cellulose nanocrystals, magnetic Fe_3O_4 nanoparticles, and *β*-cyclodextrin provided a robust, efficient, easy-to-recover adsorbent. The CNC-Fe_3O_4NP-CD nanocomposite exhibited the highest adsorption efficiency, particularly at pH 2, with a removal efficiency of 97.45%. The high efficiency of CNC-Fe_3O_4NP-CD at low pH can be attributed to the protonation of the adsorbent surface, which increased the positive charge density and enhanced the electrostatic attraction between the adsorbent and the negatively charged Cr(VI) species. This characteristic makes CNC-Fe_3O_4NP-CD particularly suitable for treating acidic wastewater, where Cr(VI) removal is often challenging due to the competition between H^+ ions and Cr(VI) for active sites. This study supports further exploration and optimization of CNC-Fe_3O_4NP-CD for practical applications in industrial wastewater treatment, where efficiency, sustainability, and cost-effectiveness are critical considerations.[94]

Acknowledgements

The authors are thankful to Maasai Mara University for offering laboratory space. The Vaal University of Technology is for analysis.

Authors contributions

Miss. Lynda Mesoppirr collected the samples, ran the experiments, and wrote the manuscript. Mr. Evans Suter assisted in sample characterization and proofreading the draft article. Dr. Wesley Omwoyo provided the chemicals, coordinated sample characterization, and proofread the draft article. Prof. N.M. Oyaro was involved in the article development, data analysis, and proofreading. Dr. S. M. Nelana facilitated sample characterization, enriched data interpretations and proofread the draft manuscript.

Disclosure statement

None of the authors disclosed any conflicting interests.

Funding

The author(s) reported there is no funding associated with the work featured in this article.

ORCID

Wesley N. Omwoyo http://orcid.org/0000-0002-0357-2405

Data availability statement

This article includes all the data generated or analyzed during this study.

References

[1] Suleiman, A. A.; Ritchie, J. T. Modeling Soil Water Redistribution during Second-Stage Evaporation. *Soil Sci. Soc. Am. J.* **2003**, *67*, 377. DOI: 10.2136/sssaj2003.0377.

[2] Qadri, R.; Faiq, M. A. Freshwater Pollution: Effects on Aquatic Life and Human Health. In *Fresh Water Pollution Dynamics and Remediation*; Qadri, H., Bhat, R.A., Mehmood, M.A., Dar, G.H., Eds. Springer Singapore: Singapore, **2020**; pp 15–26.

[3] Schwarzenbach, R. P.; Egli, T.; Hofstetter, T. B.; Von Gunten, U.; Wehrli, B. Global Water Pollution and Human Health. *Annu. Rev. Environ. Resour.* **2010**, *35*, 109–136. DOI: 10.1146/annurev-environ-100809-125342.

[4] Jayaswal, K.; Sahu, V.; Gurjar, B.R. Water Pollution, Human Health and Remediation. In *Water Remediation*; Bhattacharya, S., Gupta, A.B., Gupta, A., Pandey, A., Eds. Springer Singapore: Singapore, **2018**; pp 11–27.

[5] Verma, R.; Dwivedi, P. Heavy Metal Water pollution-A Case Study. In National Seminar on Environmental Protection and Sustainable Development. Recent Research in Science and Technology: Italy, **2013**, *5*(5), pp 98–99.

[6] Gautam, S.; Kumar, P.; Patra, A. K. Occupational Exposure to Particulate Matter in Three Indian Opencast Mines. *Air Qual. Atmos. Health* **2016**, *9*, 143–158. DOI: 10.1007/s11869-014-0311-6.

[7] Breida, M.; Younssi, S. A.; Ouammou, M.; Bouhria, M.; Hafsi, M. Pollution of Water Sources from Agricultural and Industrial Effluents: Special Attention to NO3-, Cr (VI), and Cu (II). *Water Chem.* **2019**, 39.

[8] Pathak, V.; Bhardwaj, K. K. *Industrial Waste: The Dark Side of Development*. AG Publishing House (AGPH Books): India, **2021**.

[9] Shahab, A.; Hui, Z.; Rad, S.; Xiao, H.; Siddique, J.; Huang, L. L.; Ullah, H.; Rashid, A.; Taha, M. R.; Zada, N. A Comprehensive Review on Pollution Status and Associated Health Risk Assessment of Human Exposure to Selected Heavy Metals in Road Dust across Different Cities of the World. *Environ. Geochem. Health.* **2023**, *45*, 585–606. DOI: 10.1007/s10653-022-01255-3.

[10] Jayakumar, M.; Surendran, U.; Raja, P.; Kumar, A.; Senapathi, V. A Review of Heavy Metals Accumulation Pathways, Sources and Management in Soils. *Arab. J. Geosci.* **2021**, *14*, 2156. DOI: 10.1007/s12517-021-08543-9.

[11] Ali, M. M.; Hossain, D.; Al-Imran, A.; Khan, M. S.; Begum, M.; Osman, M. H. Environmental Pollution with Heavy Metals: A Public Health Concern. In *Heavy Metals-Their Environmental Impacts and Mitigation*. IntechOpen: London, United Kingdom, **2021**, pp 771–783.

[12] Jaishankar, M.; Tseten, T.; Anbalagan, N.; Mathew, B. B.; Beeregowda, K. N. Toxicity, Mechanism and Health Effects of Some Heavy Metals. *Interdiscip. Toxicol.* **2014**, *7*, 60–72. DOI: 10.2478/intox-2014-0009.

[13] Hossini, H.; Shafie, B.; Niri, A. D.; Nazari, M.; Esfahlan, A. J.; Ahmadpour, M.; Nazmara, Z.; Ahmadimanesh, M.; Makhdoumi, P.; Mirzaei, N.; Hoseinzadeh, E. A Comprehensive Review on Human Health Effects of Chromium: Insights on Induced Toxicity. *Environ. Sci. Pollut. Res. Int.* **2022**, *29*, 70686–70705. DOI: 10.1007/s11356-022-22705-6.

[14] Qasem, N. A.; Mohammed, R. H.; Lawal, D. U. Removal of Heavy Metal Ions from Wastewater: A Comprehensive and Critical Review. *Npj Clean Water* **2021**, *4*, 1–15. DOI: 10.1038/s41545-021-00127-0.

[15] Vidu, R.; Matei, E.; Predescu, A. M.; Alhalaili, B.; Pantilimon, C.; Tarcea, C.; Predescu, C. Removal of Heavy Metals from Wastewaters: A Challenge from Current Treatment Methods to Nanotechnology Applications. *Toxics* **2020**, *8*, 101. DOI: 10.3390/toxics8040101.

[16] Bolisetty, S.; Peydayesh, M.; Mezzenga, R. Sustainable Technologies for Water Purification from Heavy Metals: Review and Analysis. *Chem. Soc. Rev.* **2019**, *48*, 463–487. DOI: 10.1039/c8cs00493e.

[17] Ahmad, A.; Azam, T. Water Purification Technologies. In *Bottled and Packaged Water*; Elsevier: Amsterdam, Netherlands, **2019**; pp 83–120.

[18] Gong, W.; Bai, L.; Liang, H. Membrane-Based Technologies for Removing Emerging Contaminants in Urban Water Systems: Limitations, Successes, and Future Improvements. *Desalination* **2024**, *590*, 117974. DOI: 10.1016/j.desal.2024.117974.

[19] Palmer, M.; Hatley, H. The Role of Surfactants in Wastewater Treatment: Impact, Removal and Future Techniques: A Critical Review. *Water Res.* **2018**, *147*, 60–72. DOI: 10.1016/j.watres.2018.09.039.

[20] Saravanan, A.; Kumar, P. S.; Hemavathy, R. V.; Jeevanantham, S.; Jawahar, M. J.; Neshaanthini, J. P.; Saravanan, R. A Review on Synthesis Methods and Recent Applications of Nanomaterial in Wastewater Treatment: Challenges and Future Perspectives. *Chemosphere* **2022**, *307*, 135713. DOI: 10.1016/j.chemosphere.2022.135713.

[21] Sun, J.; Li, X.; Quan, Y.; Yin, Y.; Zheng, S. Effect of Long-Term Organic Removal on Ion Exchange Properties and Performance during Sewage Tertiary Treatment by Conventional Anion Exchange Resins. *Chemosphere* **2015**, *136*, 181–189. DOI: 10.1016/j.chemosphere.2015.05.002.

[22] Othman, N. H.; Alias, N. H.; Fuzil, N. S.; Marpani, F.; Shahruddin, M. Z.; Chew, C. M.; David Ng, K. M.; Lau, W. J.; Ismail, A. F. A Review on the Use of Membrane Technology Systems in Developing Countries. *Membranes. (Basel)* **2021**, *12*, 30. DOI: 10.3390/membranes12010030.

[23] Shahmirzadi, M. A. A.; Hosseini, S. S.; Luo, J.; Ortiz, I. Significance, Evolution and Recent Advances in Adsorption Technology, Materials and Processes for Desalination, Water Softening and Salt Removal. *J. Environ. Manage.* **2018**, *215*, 324–344. DOI: 10.1016/j.jenvman.2018.03.040.

[24] Jaspal, D.; Malviya, A. Composites for Wastewater Purification: A Review. *Chemosphere* **2020**, *246*, 125788. DOI: 10.1016/j.chemosphere.2019.125788.

[25] Sarma, G. K.; Sen Gupta, S.; Bhattacharyya, K. G. Nanomaterials as Versatile Adsorbents for Heavy Metal Ions in Water: A Review. *Environ. Sci. Pollut. Res. Int.* **2019**, *26*, 6245–6278. DOI: 10.1007/s11356-018-04093-y.

[26] Suter, E. K.; Rutto, H. L.; Wesley, O. N.; Banza, M. Stabilized Bare Superparamagnetic Iron Oxide Nanoparticles: Synthesis and Characterization. *JNanoR.* **2023**, *80*, 81–96. DOI: 10.4028/p-f1ygDS.

[27] Wu, W.; Wu, Z.; Yu, T.; Jiang, C.; Kim, W.-S. Recent Progress on Magnetic Iron Oxide Nanoparticles: Synthesis, Surface Functional Strategies and Biomedical Applications. *Sci. Technol. Adv. Mater.* **2015**, *16*, 023501. DOI: 10.1088/1468-6996/16/2/023501.

[28] Baig, N.; Kammakakam, I.; Falath, W. Nanomaterials: A Review of Synthesis Methods, Properties, Recent Progress, and Challenges. *Mater. Adv.* **2021**, *2*, 1821–1871. DOI: 10.1039/D0MA00807A.

[29] Shrestha, S.; Wang, B.; Dutta, P. Nanoparticle Processing: Understanding and Controlling Aggregation. *Adv. Colloid Interface Sci.* **2020**, *279*, 102162. DOI: 10.1016/j.cis.2020.102162.

[30] Periasamy, R. A Systematic Review on the Significant Roles of Cyclodextrins in the Construction of Supramolecular Systems and Their Potential Usage in Various Fields. *J. Carbohydr. Chem.* **2020**, *39*, 189–216. DOI: 10.1080/07328303.2020.1792919.

[31] Chodankar, D.; Vora, A.; Kanhed, A. β-Cyclodextrin and Its Derivatives: Application in Wastewater Treatment. *Environ. Sci. Pollut. Res. Int.* **2022**, *29*, 1585–1604. DOI: 10.1007/s11356-021-17014-3.

[32] Hänninen, A.; Sarlin, E.; Lyyra, I.; Salpavaara, T.; Kellomäki, M.; Tuukkanen, S. Nanocellulose and Chitosan Based Films as Low Cost, Green Piezoelectric Materials. *Carbohydr. Polym.* **2018**, *202*, 418–424. DOI: 10.1016/j.carbpol.2018.09.001.

[33] Olivera, S.; Muralidhara, H. B.; Venkatesh, K.; Guna, V. K.; Gopalakrishna, K.; Kumar, Y. Potential Applications of Cellulose and Chitosan Nanoparticles/Composites in Wastewater Treatment: A Review. *Carbohydr. Polym.* **2016**, *153*, 600–618. DOI: 10.1016/j.carbpol.2016.08.017.

[34] Solhi, L.; Guccini, V.; Heise, K.; Solala, I.; Niinivaara, E.; Xu, W.; Mihhels, K.; Kröger, M.; Meng, Z.; Wohlert, J.; et al. Understanding Nanocellulose–Water Interactions: Turning a Detriment into an Asset. *Chem. Rev.* **2023**, *123*, 1925–2015. DOI: 10.1021/acs.chemrev.2c00611.

[35] Pandey, A.; Verma, R. K. Taxonomical and Pharmacological Status of Typha: A Review. *AnnPlSci.* **2018**, *7*, 2101–2106. DOI: 10.21746/aps.2018.7.3.2.

[36] Yamauchi, T.; Shimamura, S.; Nakazono, M.; Mochizuki, T. Aerenchyma Formation in Crop Species: A Review. *Field Crops Res.* **2013**, *152*, 8–16. DOI: 10.1016/j.fcr.2012.12.008.

[37] Mesoppirr, L. S.; Suter, E. K.; Omwoyo, W. N.; Oyaro, N. M.; Nelana, S. M. Isolative Synthesis and Characterization of Cellulose and Cellulose Nanocrystals from Typha Angustifolia. *OJAppS.* **2024**, *14*, 2443–2459. DOI: 10.4236/ojapps.2024.149161.

[38] Evans, S. K.; Wesley, O. N.; Koech, L.; Nelana, S. M.; Rutto, H. L. Structural Features of Cellulose and Cellulose Nanocrystals via In Situ Incorporation of Magnetic Iron Oxide Nanoparticles: Modification and Characterization. *Coatings* **2022**, *13*, 39. DOI: 10.3390/coatings13010039.

[39] Hassanzadeh-Tabrizi, S. A. Precise Calculation of Crystallite Size of Nanomaterials: A Review. *J. Alloys Compd.* **2023**, *968*, 171914. DOI: 10.1016/j.jallcom.2023.171914.

[40] Wiryawan, A.; Retnowati, R.; Burhan, P.; Syekhfani, S. Method of Analysis for Determination of the Chromium (Cr) Species in Water Samples by Spectrophotometry with Diphenylcarbazide. *JEEST.* **2018**, *5*, 37–46. DOI: 10.21776/ub.jeest.2018.005.01.6.

[41] Dantas, P. A.; Botaro, V. R. Synthesis and Characterization of a New Cellulose Acetate-Propionate Gel: Crosslinking Density Determination. *OJPChem.* **2012**, *02*, 144–151. DOI: 10.4236/ojpchem.2012.24019.

[42] Suter, E. K.; Rutto, H. L.; Seodigeng, T. S.; Kiambi, S. L.; Omwoyo, W. N. Green Isolation of Cellulosic Materials from Recycled Pulp and Paper Sludge: A Box-Behnken Design Optimization. *J. Environ. Sci. Health. A Tox. Hazard. Subst. Environ. Eng.* **2024**, *59*, 64–75. DOI: 10.1080/10934529.2024.2331942.

[43] Zhang, J.; Zou, W. A Novel Method for Isolating Nanocrystalline Cellulose from Eucalyptus Hardwood. *JASMI.* **2019**, *09*, 51–62. DOI: 10.4236/jasmi.2019.93006.

[44] Abdulwahid, F. S.; Haider, A. J.; Al-Musawi, S. *In Effect of Laser Parameter on Fe3O4 NPs Formation by Pulsed Laser*

Ablation in Liquid, AIP Publishing: Melville-New York, USA, **2023**.

[45] Kadam, D. M.; Kaur, A.; Kasara, A. Characterization of Natural Fibre-Based Nano-Composite Materials: A Review. *J. Agric. Eng.* **2022**, *59*, 159–178.

[46] Gala, U. *Preparation, Characterization and Dissolution Study for Curcumin-Resveratrol-Cyclodextrin Amorphous Ternary System*. Creighton University: Omaha, United States, **2015**.

[47] Tian, B.; Hua, S.; Tian, Y.; Liu, J. Cyclodextrin-Based Adsorbents for the Removal of Pollutants from Wastewater: A Review. *Environ. Sci. Pollut. Res. Int.* **2021**, *28*, 1317–1340. DOI: 10.1007/s11356-020-11168-2.

[48] Guna, V.; Ilangovan, M.; K, A.; C.v, A. K.; C.v, S.; S, Y.; Nagananda, G. S.; Venkatesh, K.; Reddy, N. Biofibers and Biocomposites from Sabai Grass: A Unique Renewable Resource. *Carbohydr. Polym.* **2019**, *218*, 243–249. DOI: 10.1016/j.carbpol.2019.04.085.

[49] Rouhou, M. C.; Abdelmoumen, S.; Thomas, S.; Attia, H.; Ghorbel, D. Use of Green Chemistry Methods in the Extraction of Dietary Fibers from Cactus Rackets (Opuntia Ficus Indica): Structural and Microstructural Studies. *Int. J. Biol. Macromol.* **2018**, *116*, 901–910. DOI: 10.1016/j.ijbiomac.2018.05.090.

[50] Tarchoun, A. F.; Trache, D.; Klapötke, T. M.; Derradji, M.; Bessa, W. Ecofriendly Isolation and Characterization of Microcrystalline Cellulose from Giant Reed Using Various Acidic Media. *Cellulose* **2019**, *26*, 7635–7651. DOI: 10.1007/s10570-019-02672-x.

[51] Chilukoti, G. R.; Mandapati, R. N. Characterization of Cellulosic Leaf Fiber from the Typha Angustifolia Plant. *J. Nat. Fib.* **2022**, *19*, 2516–2526. DOI: 10.1080/15440478.2020.1819511.

[52] Nguyen, M. D.; Tran, H.-V.; Xu, S.; Lee, T. R. Fe3O4 Nanoparticles: Structures, Synthesis, Magnetic Properties, Surface Functionalization, and Emerging Applications. *Appl. Sci.* **2021**, *11*, 11301. DOI: 10.3390/app112311301.

[53] Ding, Y.; Shen, S. Z.; Sun, H.; Sun, K.; Liu, F.; Qi, Y.; Yan, J. Design and Construction of Polymerized-Chitosan Coated Fe3O4 Magnetic Nanoparticles and Its Application for Hydrophobic Drug Delivery. *Mater. Sci. Eng. C Mater. Biol. Appl.* **2015**, *48*, 487–498. DOI: 10.1016/j.msec.2014.12.036.

[54] Falciglia, P. P.; Gagliano, E.; Scandura, P.; Bianco, C.; Tosco, T.; Sethi, R.; Varvaro, G.; Agostinelli, E.; Bongiorno, C.; Russo, A.; et al. Physico-Magnetic Properties and Dynamics of Magnetite (Fe3O4) Nanoparticles (MNPs) under the Effect of Permanent Magnetic Fields in Contaminated Water Treatment Applications. *Sep. Purif. Technol.* **2022**, *296*, 121342. DOI: 10.1016/j.seppur.2022.121342.

[55] Katiyar, V.; Dhar, P. *Cellulose Nanocrystals: Emerging Bio-Precursors for Chemical Processes*. De Gruyter: Berlin, Germany, **2020**.

[56] Chan, Y. Y.; Pang, Y. L.; Lim, S.; Chong, W. C. Facile Green Synthesis of ZnO Nanoparticles Using Natural-Based Materials: Properties, Mechanism, Surface Modification and Application. *J. Environ. Chem. Eng.* **2021**, *9*, 105417. DOI: 10.1016/j.jece.2021.105417.

[57] Marcelo, L. R.; De Gois, J. S.; Da Silva, A. A.; Cesar, D. V. Synthesis of Iron-Based Magnetic Nanocomposites and Applications in Adsorption Processes for Water Treatment: A Review. *Environ. Chem. Lett.* **2021**, *19*, 1229–1274. DOI: 10.1007/s10311-020-01134-2.

[58] Clarina, T.; Flomina, P. J.; Thangeswari, P.; Rama, V. Polpala Flower Extract Mediated One Step Green Synthesis and Characterization of Magnetite (Fe3O4) Nanoparticles. *Asia. J. Rese. Chem.* **2018**, *11*, 459–462. DOI: 10.5958/0974-4150.2018.00083.4.

[59] Ruiz-Caldas, M.-X.; Andrei, C. M.; Evans, S.; De Lannoy, C.-F. The Role of Cellulose Nanocrystals in Stabilizing Iron Nanoparticles. *Cellulose* **2020**, *27*, 8709–8724. DOI: 10.1007/s10570-020-03384-3.

[60] Hu, Q.-D.; Jiang, H.-L.; Lam, K.-H.; Hu, Z.-P.; Liu, Z.-J.; Wang, H.-Y.; Yang, Y.-Y.; Baigenzhenov, O.; Hosseini-Bandegharaei, A.; He, F.-A. Polydopamine-Modification of a Magnetic Composite Constructed from Citric Acid–Cross-Linked Cyclodextrin and Graphene Oxide for Dye Removal from Waters. *Environ. Sci. Pollut. Res. Int.* **2023**, *30*, 78521–78536. DOI: 10.1007/s11356-023-27679-7.

[61] Yuan, X.; Li, J.; Luo, L.; Zhong, Z.; Xie, X. Advances in Sorptive Removal of Hexavalent Chromium (Cr (VI)) in Aqueous Solutions Using Polymeric Materials. *Polymers (Basel)* **2023**, *15*, 388. DOI: 10.3390/polym15020388.

[62] Li, T.; Huang, X.; Wang, Q.; Yang, G. Adsorption of Metal Ions at Kaolinite Surfaces: Ion-Specific Effects, and Impacts of Charge Source and Hydroxide Formation. *Appl. Clay Sci.* **2020**, *194*, 105706. DOI: 10.1016/j.clay.2020.105706.

[63] Cruz-Lopes, L. P.; Macena, M.; Esteves, B.; Guiné, R. P. F. Ideal pH for the Adsorption of Metal Ions Cr^{6+}, Ni^{2+}, Pb^{2+} in Aqueous Solution with Different Adsorbent Materials. *Open Agric.* **2021**, *6*, 115–123. DOI: 10.1515/opag-2021-0225.

[64] Dhumal, R.; Sadgir, P. Bioadsorbents for the Removal of Salt Ions from Saline Water: A Comprehensive Review. *J. Eng. Appl. Sci.* **2023**, *70*, 80. DOI: 10.1186/s44147-023-00253-1.

[65] Suter, E.; Rutto, H.; Seodigeng, T.; Kiambi, L.; Omwoyo, W. Bagasse-Based Cellulose Nanocrystal–Magnetic Iron Oxide Nanocomposite for Removal of Chromium (VI) from Aqua Media. *Eng. Proc.* **2024**, *67*, 5.

[66] Singh, R.; Misra, V.; Singh, R. P. Synthesis, Characterization and Role of Zero-Valent Iron Nanoparticle in Removal of Hexavalent Chromium from Chromium-Spiked Soil. *J. Nanopart. Res.* **2011**, *13*, 4063–4073. DOI: 10.1007/s11051-011-0350-y.

[67] Wang, S.-L.; Lee, J.-F. Reaction Mechanism of Hexavalent Chromium with Cellulose. *Chem. Eng. J.* **2011**, *174*, 289–295. DOI: 10.1016/j.cej.2011.09.031.

[68] Suter, E.; Rutto, H.; Makomere, R.; Banza, M.; Seodigeng, T.; Kiambi, S.; Omwoyo, W. Preparation, Characterization and Application of Polymeric Ultra-Permeable Biodegradable Ferromagnetic Nanocomposite Adsorbent for Removal of Cr (VI) from Synthetic Wastewater: Kinetics, Isotherms and Thermodynamics. *Front. Environ. Chem.* **2024**, *5*, 1451262. DOI: 10.3389/fenvc.2024.1451262.

[69] Borja Ojembarrena, F. d.; Sammaraie, H.; Campano, C.; Blanco, A.; Merayo, N.; Negro, C. Hexavalent Chromium Removal from Industrial Wastewater by Adsorption and Reduction onto Cationic Cellulose Nanocrystals. *Nanomaterials (Basel)* **2022**, *12*, 4172. DOI: 10.3390/nano12234172.

[70] Wang, H.; Liu, Y.; Zeng, G.; Hu, X.; Hu, X.; Li, T.; Li, H.; Wang, Y.; Jiang, L. Grafting of β-Cyclodextrin to Magnetic Graphene Oxide via Ethylenediamine and Application for Cr (VI) Removal. *Carbohydr. Polym.* **2014**, *113*, 166–173. DOI: 10.1016/j.carbpol.2014.07.014.

[71] Liu, X.; Liu, H.; Cui, K.; Dai, Z.; Wang, B.; Weerasooriya, R.; Chen, X. Adsorption-Reduction of Cr (VI) with Magnetic Fe-CN Composites. *Water* **2023**, *15*, 2290. DOI: 10.3390/w15122290.

[72] Aigbe, U. O.; Das, R.; Ho, W. H.; Srinivasu, V.; Maity, A. A Novel Method for Removal of Cr (VI) Using Polypyrrole Magnetic Nanocomposite in the Presence of Unsteady Magnetic Fields. *Sep. Purif. Technol.* **2018**, *194*, 377–387. DOI: 10.1016/j.seppur.2017.11.057.

[73] Yu, Q.; Guo, J.; Muhammad, Y.; Li, Q.; Lu, Z.; Yun, J.; Liang, Y. Mechanisms of Enhanced Hexavalent Chromium Removal from Groundwater by Sodium Carboxymethyl Cellulose Stabilized Zerovalent Iron Nanoparticles. *J. Environ. Manage.* **2020**, *276*, 111245. DOI: 10.1016/j.jenvman.2020.111245.

[74] Kitkaew, D.; Phetrak, A.; Ampawong, S.; Mingkhwan, R.; Phihusut, D.; Okanurak, K.; Polprasert, C. Fast and Efficient Removal of Hexavalent Chromium from Water by Iron Oxide Particles. *Environm. Nat. Res. J.* **2018**, *16*.

[75] Ali, A.; Naz, S.; Mannan, A.; Shams, M. F.; Hussain, I.; Zia, M. Adsorption of Ni2+, Hg2+, Pb2+, Cr3+, and Co2+ on Iron Oxide Nanoparticles Immobilized on Cellulose Fiber:

Equilibrium, Kinetic, Thermodynamic, Mechanisms, and Statistical Supposition. *Desalin. Water Treat.* **2017**, *95*, 234–246. DOI: 10.5004/dwt.2017.21560.

[76] Samrot, A. V.; Shobana, N.; Durga Sruthi, P.; Sahithya, C. S. Utilization of Chitosan-Coated Superparamagnetic Iron Oxide Nanoparticles for Chromium Removal. *Appl. Water Sci.* **2018**, *8*, 1–19. DOI: 10.1007/s13201-018-0841-4.

[77] Wang, T.; Liu, Y.; Wang, J.; Wang, X.; Liu, B.; Wang, Y. In-Situ Remediation of Hexavalent Chromium Contaminated Groundwater and Saturated Soil Using Stabilized Iron Sulfide Nanoparticles. *J. Environ. Manage.* **2019**, *231*, 679–686. DOI: 10.1016/j.jenvman.2018.10.085.

[78] Jawed, A.; Golder, A. K.; Pandey, L. M. Bio-Based Iron Oxide Nanoparticles Forming bi-Functional Chitosan Composite Adsorbent for Cr (VI) Decontamination. *Chem. Eng. J.* **2024**, *481*, 148411. DOI: 10.1016/j.cej.2023.148411.

[79] Zhao, L.; Zhao, Y.; Yang, B.; Teng, H. Application of Carboxymethyl Cellulose–Stabilized Sulfidated Nano Zerovalent Iron for Removal of Cr(VI) in Simulated Groundwater. *Water. Air. Soil Pollut.* **2019**, *230*, 113. DOI: 10.1007/s11270-019-4166-1.

[80] Biswas, S.; Meikap, B. C.; Sen, T. K. Adsorptive Removal of Aqueous Phase Copper (Cu 2+) and Nickel (Ni 2+) Metal Ions by Synthesized Biochar–Biopolymeric Hybrid Adsorbents and Process Optimization by Response Surface Methodology (RSM). *Water. Air. Soil Pollut.* **2019**, *230*, 1–23. DOI: 10.1007/s11270-019-4258-y.

[81] Singh, J.; Mishra, V. Development of Sustainable and Ecofriendly Metal Ion Scavenger for Adsorbing Cu2+, Ni2+ and Zn2+ Ions from the Aqueous Phase. *Sep. Sci. Technol.* **2022**, *57*, 354–371. DOI: 10.1080/01496395.2021.1913421.

[82] Singh, J.; Mishra, V. Simultaneous Removal of Cu^{2+}, Ni^{2+} and Zn^{2+} Ions Using Leftover *Azadirachta Indica* Twig Ash. *Biorem. J.* **2021**, *25*, 48–71. DOI: 10.1080/10889868.2020.1843394.

[83] Salehi, M.; Sharafoddinzadeh, D.; Mokhtari, F.; Esfandarani, M. S.; Karami, S. Electrospun Nanofibers for Efficient Adsorption of Heavy Metals from Water and Wastewater. **2021**. DOI: 10.3934/ctr.2021001.

[84] Wang, J.; Guo, X. Adsorption Kinetics and Isotherm Models of Heavy Metals by Various Adsorbents: An Overview. *Crit. Rev. Environ. Sci. Technol.* **2023**, *53*, 1837–1865. DOI: 10.1080/10643389.2023.2221157.

[85] Chaudhary, M.; Singh, L.; Rekha, P.; Srivastava, V. C.; Mohanty, P. Adsorption of Uranium from Aqueous Solution as Well as Seawater Conditions by Nitrogen-Enriched Nanoporous Polytriazine. *Chem. Eng. J.* **2019**, *378*, 122236. DOI: 10.1016/j.cej.2019.122236.

[86] Rani, S.; Sharma, S.; Bansal, M.; Garg, R.; Garg, R. Enhanced Zn (II) Adsorption by Chemically Modified Sawdust Based Biosorbents. *Environ. Sci. Pollut. Res.* **2022**, *30*, 99046–99061. DOI: 10.1007/s11356-022-22963-4.

[87] Pholosi, A.; Naidoo, E. B.; Ofomaja, A. E. Intraparticle Diffusion of Cr(VI) through Biomass and Magnetite Coated Biomass: A Comparative Kinetic and Diffusion Study. *South Afr. J. Chem. Eng.* **2020**, *32*, 39–55. DOI: 10.1016/j.sajce.2020.01.005.

[88] Sarode, D. B.; Jadhav, R. N.; Khatik, V. A.; Ingle, S. T.; Attarde, S. B. Extraction and Leaching of Heavy Metals from Thermal Power Plant Fly Ash and Its Admixtures. *Pol. J. Environ. Stud.* **2010**, *19*, 1325–1330.

[89] Nag, S.; Mondal, A.; Mishra, U.; Bar, N.; Das, S. K. Removal of Chromium(VI) from Aqueous Solutions Using Rubber Leaf Powder: Batch and Column Studies. *Desalin. Water Treat.* **2016**, *57*, 16927–16942. DOI: 10.1080/19443994.2015.1083893.

[90] Mitra, T.; Bar, N.; Das, S. K. Rice Husk: Green Adsorbent for Pb(II) and Cr(VI) Removal from Aqueous Solution—Column Study and GA–NN Modeling. *SN Appl. Sci.* **2019**, *1*, 486. DOI: 10.1007/s42452-019-0513-5.

[91] Tumolo, M.; Ancona, V.; De Paola, D.; Losacco, D.; Campanale, C.; Massarelli, C.; Uricchio, V. F. Chromium Pollution in European Water, Sources, Health Risk, and Remediation Strategies: An Overview. *Int. J. Environ. Res. Public Health.* **2020**, *17*, 5438. DOI: 10.3390/ijerph17155438.

[92] Ullah, S.; Liu, Q.; Wang, S.; Jan, A. U.; Sharif, H. M. A.; Ditta, A.; Wang, G.; Cheng, H. Sources, Impacts, Factors Affecting Cr Uptake in Plants, and Mechanisms behind Phytoremediation of Cr-Contaminated Soils. *Sci. Total Environ.* **2023**, *899*, 165726. DOI: 10.1016/j.scitotenv.2023.165726.

[93] Yu, D. Chromium Toxicity. **2008**.

[94] Zhao, X.; Lv, L.; Pan, B.; Zhang, W.; Zhang, S.; Zhang, Q. Polymer-Supported Nanocomposites for Environmental Application: A Review. *Chem. Eng. J.* **2011**, *170*, 381–394. DOI: 10.1016/j.cej.2011.02.071.